Parsimonious inertial cavitation rheometry via bubble collapse time

Zhiren Zhu*[a], Sawyer Remillard*[b], Bachir A. Abeid[a], Danila Frolkin[c], Spencer H. Bryngelson[d,e,f], Jin Yang[c], Mauro Rodriguez Jr.[b], Jonathan B. Estrada[a]

[a]*Department of Mechanical Engineering, University of Michigan, Ann Arbor, 48105, MI, USA*

[b]*School of Engineering, Brown University, Providence, 02912, RI, USA*

[c]*Department of Aerospace Engineering and Engineering Mechanics, The University of Texas at Austin, Austin, 78712, TX, USA*

[d]*School of Computational Science and Engineering, Georgia Institute of Technology, Atlanta, 30332, GA, USA*

[e]*Daniel Guggenheim School of Aerospace Engineering, Georgia Institute of Technology, Atlanta, 30332, GA, USA*

[f]*George W. Woodruff School of Mechanical Engineering, Georgia Institute of Technology, Atlanta, 30332, GA, USA*

Abstract

The rapid and accurate characterization of soft, viscoelastic materials at high strain rates is of interest in biological and engineering applications such as assessing the extent of non-invasive tissue surgery completion and developing injury criteria for the mitigation of blast injuries. The inertial microcavitation rheometry technique (IMR, Estrada et al., 2018) allows for the minimally invasive characterization of local viscoelastic properties at strain rates up to 10^8/s. However, IMR relies on bright-field videography of a sufficiently translucent sample at approximately 1 million frames per second and a simulation-dependent fit optimization process that can require hours of post-processing. We present an IMR-style technique that parsimoniously characterizes viscoelastic models. The approach uses experimental advancements to accurately estimate the time to first collapse of the laser-induced cavity. A theoretical energy balance analysis yields an approximate collapse time based on the material viscoelasticity parameters. The method closely matches the accuracy of the original IMR procedure while decreasing the computational cost from hours to seconds for the Kelvin–Voigt model and potentially reducing dependence on high-speed videography. This technique can enable nearly real-time characterization of a broader range of soft, viscoelastic hydrogels and biological materials.

Keywords: Viscoelastic material, mechanical testing, high strain rate
PACS: 0000, 1111
2000 MSC: 0000, 1111

1. Introduction

The characterization of viscoelastic soft materials undergoing fast, finite deformations is necessary for a wide range of applications, including design against biological tissue or scaffold damage in injury [1, 2], non-invasive ultrasound- [3–5], and laser-based surgery techniques [6]. However, soft materials such as hydrogels are challenging to characterize due to their small elastic modulus, which ranges from 100 Pa to 1 MPa, and the difficulties of gripping and manipulating the specimens during experiments. Due to the slow wave speeds associated with high compliance, traditional high-strain rate experiments such as the Kolsky bar must be enhanced with pulse shaping, weak signal

sensing, and other complicating techniques when applied to the characterization of soft materials [7]. Moreover, hydrogels can be 3D printed using advanced additive manufacturing techniques with spatially dependent microstructure. Soft biological tissues often exhibit spatial heterogeneity, making it challenging to measure their material property distribution with conventional methods that only provide a macroscale average modulus.

A family of alternative techniques uses local cavity expansion to assess the finite deformation behaviors of hydrogels. Crosby et al. first developed needle-induced cavitation rheology as an approach to probe the local elastic properties of soft materials [8, 9]. A cavity of air or immiscible liquid is injected into the characterized media. The elastic modulus is determined from the pressure and bubble radius at the onset of mechanical instability. This quasi-static approach has been extended in recent years to a ballistic strain-rate regime of approximately $10^4\,\mathrm{s}^{-1}$ by Milner and Hutchens [10, 11]. Cohen and co-workers introduced the capability to cyclically expand and relax the needle-induced cavity at controlled stretch rates [12, 13], enabling finite deformation characterization of viscoelastic materials. The inertial microcavitation rheometry (IMR) technique, introduced by Estrada et al. [14] and improved by others recently [15–17], accesses a higher range of strain rate by using laser-induced cavitation (LIC) in a soft material. An ultra-high-speed camera images the bubble kinematics and the viscoelastic properties of the cavitated media are inversely characterized according to an inertial cavitation bubble model [18] with refinements accounting for a two-component mixture of bubble content with heat diffusion and mass transfer [19–22] and stress field in the surrounding media [23–26].

IMR inversely characterizes viscoelasticity at strain rates reaching 10^8/s but has only been successfully applied to characterize nearly transparent materials. The reliance on high-speed, bright-field videography of the cavity restricts the optical turbidity of the characterized material. Furthermore, the computational cost of the forward simulation, optimization, and best-fit procedure is not computationally tractable for on-the-fly characterization. Each forward simulation requires about ten seconds. Batch-fitting multiple experiments simultaneously and increasing the number of model parameters cause an exponential increase in the required forward simulations. If the simulations were run on demand, additional complexity would make calibration time intractable.

We develop a strategy for the parsimonious characterization of viscoelastic models. The strategy leverages high-fidelity measurements of the maximum bubble radius, the long-term equilibrium bubble radius, and the time from maximum expansion to primary bubble collapse. These quantities of interest relate distinctly to the ultra-high-rate elastic and viscous behaviors of soft hydrogels. In Section 2, we present an LIC experiment setup capable of quantifying the time of collapse to an accuracy of approximately 20 ns. The experiments are complemented with an energy balance analysis that allows the approximate quantification of the effects of material viscoelasticity, surface tension, bubble pressure, and finite material wave speed on the time to the first bubble collapse. We then introduce the parsimonious inertial microcavitation (pIMR) procedure enabled by these experimental and theoretical advancements. In Section 3, we verify the energy balance analysis approximation of collapse time as a basis for the proposed characterization strategy. We demonstrate in Section 4 high-fidelity viscoelastic model parameterization from tens of experiments with computational post-processing that takes only seconds. In Section 5, we discuss the implications of the results obtained and the limitations of the proposed strategy. We provide concluding remarks in Section 6.

2. Theory and Methods

2.1. Full-physics model of bubble dynamics

The theory derived in the preceding work and briefly described here will be referred to as the full-physics model of bubble dynamics.[1] A more thorough discussion of the theory, including its underlying assumptions and regimes of applicability, can be found in Estrada et al. [14]. This model considers a spherical bubble in an infinite surrounding material environment subjected to a pressure change that causes rapid radial motion. We assume that the bubble contains a mixture of condensible water vapor and other gases modeled as non-condensible. The material outside the cavity is viscoelastic and approximated as nearly incompressible. That is, the kinematic deformation field is volume-preserving and permits outgoing acoustic waves with a finite speed. The initial growth phase of a bubble induced by a pulsed laser involves complex plasma physics. Rather than directly modeling this growth, we assume thermodynamic equilibrium between the gas contents and the surrounding medium at maximum bubble expansion.

The modified Keller–Miksis equation [14, 18] describes the bubble radius behavior as

$$\left(1 - \frac{\dot{R}}{c}\right) R\ddot{R} + \frac{3}{2}\left(1 - \frac{\dot{R}}{3c}\right)\dot{R}^2 = \frac{1}{\rho}\left(1 + \frac{\dot{R}}{c}\right)\left(p_{\mathrm{b}} - \frac{2\gamma}{R} + S - p_\infty\right) + \frac{1}{\rho}\frac{R}{c}\overline{\left(p_{\mathrm{b}} - \frac{2\gamma}{R} + S\right)}, \quad (1)$$

where overdots denote derivatives with respect to time t, R the evolving bubble radius, ρ the mass density of the surrounding material, c the longitudinal wave speed, γ the bubble wall surface tension, p_{b} the internal bubble pressure, p_∞ the far-field pressure, and S the stress integral defined as

$$S = \int_R^\infty \frac{2}{r}\left(s_{rr} - s_{\theta\theta}\right)\mathrm{d}r, \quad (2)$$

where s_{rr} and $s_{\theta\theta}$ are the normal radial and normal circumferential components of $\mathbf{s}$, the deviatoric part of the Cauchy stress in the surrounding material. Mass and heat transfer of the two-phase bubble contents are assumed to obey Fick's and Fourier's laws, resulting in a set of PDEs. Following Estrada et al. [14], numerical solutions to the modified Keller–Miksis equation coupled with the bubble content equations are obtained with the `ode23tb` function in MATLAB (The MathWorks, Inc., Natick, MA).

2.1.1. Non-dimensionalization and solution of bubble dynamics model

We follow existing work to non-dimensionalize the governing equations and clarify the interactions between material parameters [14]. We define a characteristic velocity $v_{\mathrm{c}} = \sqrt{p_\infty/\rho}$ and construct dimensionless quantities, as shown in table 1. The non-dimensional Keller–Miksis equation describing the evolution of the non-dimensional bubble radius R^* is

$$\left(1 - \frac{\dot{R}^*}{c^*}\right) R^*\ddot{R}^* + \frac{3}{2}\left(1 - \frac{\dot{R}^*}{3c^*}\right)\dot{R}^{*2} =$$
$$\left(1 + \frac{\dot{R}^*}{c^*}\right)\left(p_{\mathrm{b}}^* - \frac{1}{\mathrm{We}\,R^*} + S^* - 1\right) + \frac{R^*}{c^*}\overline{\left(p_{\mathrm{b}}^* - \frac{1}{\mathrm{We}\,R^*} + S^*\right)}. \quad (3)$$

---

[1]We acknowledge that this model is "full" only in the sense that it contains a set of physical phenomena that faithfully represent the problem at hand.

Table 1: Dimensionless quantities in the Keller–Miksis Equation.

Dimensional quantity	Dimensionless quantity	Name
t	$t^* = t\, v_c/R_{\max}$	Time
R	$R^* = R/R_{\max}$	Bubble-wall radius
R_0	$R_0^* = R_0/R_{\max}$	Equilibrium bubble-wall radius
c	$c^* = c/v_c$	Material wave speed
p_b	$p_b^* = p_b/p_\infty$	Bubble pressure
γ	$\mathrm{We} = p_\infty R_{\max}/(2\gamma)$	Weber number
S	$S^* = S/p_\infty$	Stress integral
G	$\mathrm{Ca} = p_\infty/G$	Cauchy number
μ	$\mathrm{Re} = \rho v_c R_{\max}/\mu$	Reynolds number
$\tau_1 = \mu/G_1$	$\mathrm{De} = \mu v_c/(G_1 R_{\max})$	Deborah number

Table 2: Summary of material stress integrals.

Material model	Stress integral relationship S^*
Neo-Hookean	$S_{NH}^* = [4(R_0^*/R^*) + (R_0^*/R^*)^4 - 5]/(2\,\mathrm{Ca})$
Newtonian	$S_v^* = -(4/\mathrm{Re})\dot{R}^*/R^*,$
Kelvin–Voigt	$S_{KV}^* = S_v^* + S_{NH}^*$
Maxwell	$\mathrm{De}\dot{S}_m^* + S_m^* = -(4/\mathrm{Re})\dot{R}^*/R^*$
Standard linear solid (SLS)	$S_{SLS}^* = S_m^* + S_{NH}^*$

Unless stated otherwise, we assume $\rho = 998.2\,\mathrm{kg/m^3}$, $p_\infty = 101.3\,\mathrm{kPa}$, $c = 1484\,\mathrm{m/s}$, and $\gamma = 0.072\,\mathrm{N/m}$ in the ensuing calculation. For the mixture of water and poly(ethylene glycol) diacrylate (PEGDA) characterized in Section 4.2, we assume $\rho = 1100\,\mathrm{kg/m^3}$.

2.1.2. Stress integral in the surrounding medium

The stress integral S^* for the viscoelastic constitutive models considered in this work are tabulated in table 2. We consider constitutive models with stress responses that are additively decomposed into those of three elementary components: a neo-Hookean hyperelastic contribution, a Newtonian viscous contribution, and a Maxwell fading memory viscoelastic contribution. The stress integral results for the Kelvin–Voigt viscoelastic models follow our previous work [14], where the Kelvin–Voigt model consists of parallel neo-Hookean and Newtonian responses. The stress integral for the Maxwell model is derived in Appendix A. The standard linear solid (SLS) model consists of a neo-Hookean response parallel to a Maxwell response. These models have been demonstrated to characterize hydrogels with IMR to date [14, 15, 27].

Here, we are primarily interested in the contribution of material viscoelasticity to the collapse time. These contributions show up in the form of the Cauchy number, Ca, the Reynolds number, Re, and the Deborah number, De. Ca is inversely proportional to the ground-state elastic shear modulus, G. Re is inversely proportional to the viscosity, μ, but also dependent on the size scale of the cavitation. The viscous contribution of a material varies when viscosity μ is held constant, but the characteristic length scale $R_{\max}$ is adjusted. De reflects a relative time scale of the Maxwell-type exponential relaxation of the material. When $\mathrm{De} \to 0$ while Re is held constant, the viscoelastic relaxation occurs much more rapidly than the bubble dynamics, and the viscous contribution is effectively that of a Newtonian fluid. When $\mathrm{De} \to \infty$ while Re is held constant, the relaxation occurs much more slowly than the bubble dynamics, and the fluid is inviscid.

2.2. Energy balance analysis and analytical estimates of collapse time

The dependence of the Keller–Miksis equation (3) on the stress integral and its derivative has an important result on the dynamic evolution of the system. In particular, material elasticity stores potential energy in the system during bubble expansion; this energy is released during bubble contraction and accelerates the bubble inward toward collapse. In contrast, material viscosity acts as a damper that slows the rate of bubble motion. For both scenarios, it is useful to have a benchmark collapse time, which is the time to closure without the effects mentioned above, in which the liquid pressure is the only driving force. We compare additional mechanical and physical effects with this time.

This benchmark time is commonly called the Rayleigh collapse time [28]. Lord Rayleigh arrived at this characteristic time through an energy analysis with four assumptions: the bubble has no contents, there is no surface tension between the void and the surrounding material, and the surrounding material is incompressible and inviscid. As a consequence of these assumptions, the potential and kinetic energy of the surrounding material dictate the evolution of the bubble radius. The Keller–Miksis equation (3) simplifies without the finite wave speed, material behavior, or bubble contents to

$$R^* \ddot{R}^* + \frac{3}{2} \dot{R}^{*2} = -1. \tag{4}$$

The potential energy of the inviscid liquid surrounding the bubble is the volume integral of the non-dimensional liquid pressure,

$$E_{\text{LP}}^* = \int_{V_b^*} \mathrm{d}V^* = V_b^*, \tag{5}$$

where V_b^* is the volume of the bubble. The kinetic energy of the liquid is

$$E_{\text{LK}}^* = \int_{V_l^*} \frac{1}{2} u_r^{*2} \mathrm{d}V^* = \int_{V_l^*} \frac{1}{2} \left(\frac{R^{*2} \dot{R}^*}{r^{*2}} \right)^2 \mathrm{d}V^* = 2\pi R^{*3} \dot{R}^{*2}. \tag{6}$$

For Lord Rayleigh's estimate, the void begins at rest, corresponding to an initial kinetic energy of zero. The energy balance is then $(4\pi/3)(R^{*3} - 1) + 2\pi R^{*3} \dot{R}^{*2} = 0$. Isolating the bubble wall velocity as a function of the radius, $\dot{R}^*(R^*(t^*))$, invert, and integrate to the closure of the bubble, we obtain the Rayleigh collapse time

$$t_{\text{RC}}^* = \int_1^0 -\left[-\frac{2}{3} \left(1 - \frac{1}{R^{*3}} \right) \right]^{-1/2} \mathrm{d}R^* = \sqrt{\frac{3\pi}{2}} \frac{\Gamma[5/6]}{\Gamma[1/3]} \approx 0.91468. \tag{7}$$

To obtain the dimensional form, we multiply by the characteristic timescale, $R_{\max}\sqrt{\rho/p_\infty}$. The dimensional Rayleigh collapse time depends on the material density ρ and the maximum bubble radius $R_{\max}$, often observed in experiments.

Although Lord Rayleigh's limiting case is important, the real collapse time of a bubble in a soft material also depends on the bubble pressure, surface tension, finite wave speed, and viscoelastic properties of the surrounding material. Here, we develop upon and extend existing theory for an approximate modified Rayleigh collapse time for soft material characterization.

Phenomenon	Function modifying Rayleigh–Plesset equation f^*
Bubble pressure	$f_{bc}^* = p_b^* = p_{go}^*(R_0/R^*)^{*\,3\kappa} + p_{v,sat}^*$
Weak compressibility	$f_{wc}^* = (\dot{R}^*/c_m^*)R^*\ddot{R}^* + (\dot{R}^*/2\,c_m^*)\dot{R}^{*2} - \dot{R}^*/c_m^*$
Surface tension	$f_{We}^* = -1/(We\,R^*)$
Material response	$f_S^* = S^*$
Compressibility affecting bubble pressure	$f_{cbc}^* = \dot{R}^* p_b^*/c_m^* + R^*/\dot{p}_b^* c_m^*$
Compressibility affecting material response	$f_{cS}^* = \dot{R}^* S^*/c_m^* + R^*\dot{S}^*/c_m^*$

Table 3: Physical phenomena and corresponding functional changes to the Rayleigh–Plesset equation. The right-most column sums to the overall function that transforms (8) into (3) (under the polytropic gas assumption).

2.2.1. General approach for modified Rayleigh collapse time

Lord Rayleigh's approach is fundamental to the bubble collapse problem. To account for subsequent changes to the collapse dynamics caused by additional physics relevant to our specific problems, we can generalize a Rayleigh-type model as

$$R^*\ddot{R}^* + \frac{3}{2}\dot{R}^{*2} = -1 + f^*(R^*, \dot{R}^*, \ddot{R}^*, S^*, c_m^*, R_0^*, p_b^*, \dots). \tag{8}$$

The functional form of f^* varies for models of different physical phenomena (see table 3). Eq. (3) is the sum of the terms in the right column of table 3.

We consider a constant f^* value without loss of generality. The later effect on the collapse time is similar to that of changing the ambient pressure on the system. Therefore, we propose a linearization of these terms to obtain an approximate modified collapse time. The aim is to determine the mean value of the function f^* during the first collapse, $\overline{f}^*$, such that we obtain a time-averaged force, or resistance to force, acting on the bubble from the surrounding environment. To solve for the modification factor $\overline{f}^*$, we define a time-averaged value of the function f^* as

$$\overline{f}^* = \frac{1}{t_c^*}\int_0^{t_c^*} f^*\,dt^* = \frac{1}{t_c^*}\int_1^0 \frac{f^*}{\dot{R}^*}\,dR^*. \tag{9}$$

We make the following ansatz for the reduction in the liquid potential due to this modification, $E_f^* = -(4\pi/3)\overline{f}^* R^{*3}$, and the resulting energy balance is

$$\frac{4}{3}\pi\left(1 - \overline{f}^*\right)(R^{*3} - 1) + 2\pi\rho R^{*3}\dot{R}^{*2} = 0. \tag{10}$$

Following the procedure of Lord Rayleigh, the approximate bubble wall velocity is

$$\dot{R}^* \approx -\left[\frac{2}{3}\left(1 - \overline{f}^*\right)\left(\frac{1}{R^{*3}} - 1\right)\right]^{1/2}, \tag{11}$$

with the general approximate modified collapse, time

$$t_c^* \approx \int_{R_{max}}^0 -\left[-\frac{2}{3}\left(1 - \overline{f}^*\right)\left(1 - \frac{1}{R^{*3}}\right)\right]^{-1/2} dR^* = t_{RC}^*\left(1 - \overline{f}^*\right)^{-1/2}. \tag{12}$$

To consider the effects within the governing equation, (3), equation (12) Therefore, we can write the modification factor to be equal to the following, $\overline{f}^* = \sum_\alpha \overline{f}_\alpha^*$, where α is indexing physical

effects modeled within the numerical simulations. We will consider each of the constitutive terms in equation (3) individually. We consider the dominant effect of the collapse time to be the inertial effect, governed by the ODE of the void collapse in (8); terms that involve compressibility interacting with other physical phenomena are second-order and will be neglected. Additionally, for simplicity, this analysis will neglect heat and mass transfer in and outside the bubble.

2.2.2. Effect of pressure due to bubble contents

We assume that there are two primary gases inside the bubble: (1) water vapor and (2) a non-water gas phase consisting of air and vaporized material that diffuses back into the material over time scales much longer than the one considered here for the inertial dynamics event. During bubble collapse, the bubble pressure increases as the volume decreases. Bubble pressure acts as a resistive force to the pressure-driven collapse, prolonging the instance of minimum volume.

We consider the bubble pressure as the sum of partial pressures of the gases present [29]: $p_b^* = p_v^* + p_{go}^*(R_0^*/R^*)^{3\kappa}$, where R_0^* is the equilibrium bubble radius, and κ the ratio of the heat capacity at constant pressure, C_P, to the heat capacity at constant volume, C_V. Here, we assume the water vapor to be p_v^* and the non-condensible gas to be polytropic, where p_{go}^* is the equilibrium bubble pressure. The integral to evaluate the mean value of the bubble pressure is non-convergent for the $\lim_{R^* \to 0}$ since this corresponds to infinite bubble pressure. Furthermore, there is no expression available for $R_{\min}$ such that we could obtain a finite integrated result. Since $f_{bc}^* \propto p_{go}^* R_0^{*3\kappa}$, then $\overline{f}_{bc}^* \propto p_{go}^* R_0^{*3\kappa}$ and so a proportionality constant results from linearization through integration of $R(t)$ such that $\overline{f}_{bc}^* = \mathcal{B}p_{go}^* R_0^{*3\kappa} + p_v^*$. The value of $\mathcal{B}$ is obtained by numerically solving the exact collapse time integral. When solving for this proportionality, we neglect the effect of water vapor inside the bubble, as its effect on the collapse time is additive to that of the non-water gas phase. The exact collapse time is found by considering the resistive force provided by the bubble contents to prevent collapse. The bubble's internal energy, or the reduction of liquid potential energy associated with the presence of bubble contents, is

$$E_{\mathrm{BIE}}^* = \int_{V_b^*} -p_b^* dV^* = \int_{V_b^*} -p_{go}^* \left(\frac{V_0^*}{V_b^*}\right)^\kappa dV^* = \frac{p_b^* V_b^*}{\kappa - 1}. \tag{13}$$

For the special (isothermal) case of $\kappa = 1$, we obtain the following form of the energy:

$$E_{\mathrm{BIE}}^* = -\frac{4}{3}\pi R_0^{*3} p_{go}^* \log\left[\frac{4}{3}\pi R^{*3}\right]. \tag{14}$$

The non-dimensional exact collapse time is

$$t_c^* = \begin{cases} \displaystyle\int_1^{R_{\min}^*} -\sqrt{\frac{3}{2}}\left[\frac{1}{R^{*3}}\left(1 + \frac{p_{go}^* R_0^{*3\kappa}}{\kappa - 1} - \frac{p_{go}^* R^{*3}}{\kappa - 1}\left(\frac{R_0^*}{R^*}\right)^{3\kappa} - R^{*3}\right)\right]^{-1/2} dR^*, & \text{for } \kappa \neq 1, \\[2em] \displaystyle\int_1^{R_{\min}^*} -\sqrt{\frac{3}{2}}\left[p_{go}^* R_0^{*3}\frac{\log\left(R^{*3}\right)}{R^{*3}} + \frac{1}{R^{*3}} - 1\right]^{-1/2} dR^*, & \text{for } \kappa = 1. \end{cases} \tag{15}$$

We evaluate (15) for a single, small (0.01) non-dimensional equilibrium radius. The integral is evaluated by setting the minimum radius to zero and taking the real part of the result because any radii smaller than the minimum radius will produce imaginary contributions. For the special cases of $\kappa = 1.4$ (isentropic) and $\kappa = 1$, we obtain $\mathcal{B} = 2.1844$ and 1.4942.

Simulations with the full-physics bubble dynamics model show that the heat transfer and mass diffusion of the water vapor have negligible effects on the early stage of the initial collapse. We thus assume that the water vapor can also be considered non-condensible during the bubble collapse, and the mixture undergoes an isothermal process corresponding to $\kappa = 1$. The initial partial pressure of the water vapor is $p^*_{\mathrm{v,sat}} = 0.0308$, following an empirical estimate of the saturated vapor pressure at ambient temperature [14, 30]. We correct the earlier result for a vapor-free bubble if the long-term equilibrium pressure of the non-vapor gas is $p^*_{\mathrm{go}} = 1$. This correction gives the average effect of the two-phase bubble pressure on the collapse time, $\overline{f}^*_{\mathrm{bc}} = \mathcal{B}\left(p^*_{\mathrm{go}} R^{*\ 3}_0 + p^*_{\mathrm{v,sat}}\right)$.

2.2.3. Weak compressibility effects

The third term of f^*_{wc} in table 3 dominates the weak compressibility effect. This term is linear and dominates for the length and time scales of inertial microcavitation collapse events. Thus, $f^*_{\mathrm{wc}} \approx -M_c \dot{R}^*$, where $M_c = 1/c^*_{\mathrm{m}}$ is the characteristic Mach number. Time averaging f^*_{wc} for the duration of the collapse and solving explicitly,

$$\overline{f}^*_{\mathrm{wc}} = \frac{(1 - \overline{f}^*_c)^{1/2}}{t^*_{\mathrm{RC}}} \int_1^0 -M_c \mathrm{d}R^* = M_c \frac{(1 - \overline{f}^*_{\mathrm{wc}})^{1/2}}{t^*_{\mathrm{RC}}} = \frac{2M_c}{M_c + \sqrt{M_c^2 + 4t^{*2}_{\mathrm{RC}}}}. \tag{16}$$

2.2.4. Surface tension effects

The surface tension of the water-containing material plays a non-negligible role during the collapse. Surface tension acts as a driving force toward collapse. Time-averaging the surface tension modification function from table 3 to get an approximate linear form,

$$\overline{f}^*_{\mathrm{We}} = \frac{(1 - \overline{f}^*_{\mathrm{We}})^{1/2}}{t^*_{\mathrm{RC}}} \int_1^0 \frac{1}{\mathrm{We}\, R^*} \left[\frac{2}{3}\left(1 - \overline{f}_{\mathrm{We}*}\right)\left(\frac{1}{R^{*3}} - 1\right)\right]^{-1/2} \mathrm{d}R^* = \frac{-\pi}{\sqrt{6}\,\mathrm{We}\, t^*_{\mathrm{RC}}}. \tag{17}$$

2.3. Stress integral considerations

The material's elastic and viscous behavior speeds up and slows down the collapse event, respectively. Recent work by the authors [31] obtained an expression for the collapse time of a void surrounded by a neo-Hookean elastic material. We build on this result and consider more general viscoelastic models. For the linear viscoelastic materials considered here, the general linear constitutive model relating the stress to the strain is $\mathrm{De}\dot{s}^* + s^* = 2\left(\varepsilon^*/\mathrm{Ca} + \dot{\varepsilon}^*/\mathrm{Re}\right)$. In the case of a non-linear elastic material, the relationship for the stress is found through a strain energy density function. The stress integral $f^* = S^*$ determines the effect of the material response on the bubble dynamics.

2.3.1. Neo-Hookean elasticity

Approaching bubble closure, $R^*_0 \to 0$, the neo-Hookean stress integral converges to a constant, $\overline{f}^*_{\mathrm{NH}} = -5/2\,\mathrm{Ca}$. Substituting the neo-Hookean expression for $\overline{f}^*_{\mathrm{NH}}$ into (12) results in the modified collapse time consistent with the result in Yang et al. [31]. That is, $t^*_c = t^*_{\mathrm{RC}}(1 + 5/2\,\mathrm{Ca})^{-1/2}$. However, from examining the stress integral in table 3, for finite R^*_0 and small Cauchy number, the term that is linear in R^*_0 can no longer be assumed to be small. For the inertial microcavitaiton events of interest, R^*_0 tends to be around 0.1–0.25, thus we neglect the term that is quartic in R^*_0 for the following analysis. Therefore, f^*_{NH} becomes $f^*_{\mathrm{NH}} = (R^*_0/R^* - 5)/2\,\mathrm{Ca}$. The first-order correction to finite equilibrium bubble radius follows as

$$\overline{f}^*_{\mathrm{NH}} = \frac{1}{t^*_{\mathrm{RC}}} \int_1^0 \frac{1}{2\mathrm{Ca}} \left[4\frac{R^*_0}{R^*} - 5\right]\left[\frac{2}{3}\left(\frac{1}{R^{*3}} - 1\right)\right]^{-1/2} \mathrm{d}R^* = \frac{1}{\mathrm{Ca}}\left(\sqrt{\frac{2}{3}}\frac{R^*_0 \pi}{t^*_{\mathrm{RC}}} - \frac{5}{2}\right). \tag{18}$$

8

2.3.2. Viscous Newtonian Fluid

Unlike the elastic case, the mean value for a viscous Newtonian fluid is non-convergent. Thus, we introduce a proportionality constant for $\overline{f}_v^*$ that depends on the Reynolds number, $\mathcal{C}(\mathrm{Re})$, such that

$$\overline{f}_v^* = \frac{4\left(1-\overline{f}_v^*\right)^{1/2}}{\mathrm{Re}\, t_{\mathrm{RC}}^*} \lim_{R_{\min}^* \to 0} \int_1^{R_{\min}^*} -\frac{1}{R^*}\mathrm{d}R^* \approx \frac{-4\mathcal{C}\left(1-\overline{f}_v^*\right)^{1/2}}{t_{\mathrm{RC}}^*\,\mathrm{Re}}. \tag{19}$$

After bounding this integral, implicit relationship of $\overline{f}_v^*$ simplifies to,

$$\overline{f}_v^* = \frac{4\mathcal{C}}{2\mathcal{C} + \sqrt{\mathrm{Re}^2\, t_{\mathrm{RC}}^{*2} + 4\mathcal{C}^2}}. \tag{20}$$

$\mathcal{C}$ is obtained by relating the approximation of the collapse time to the exact definition of the viscous collapse time.

The collapse time within a viscous fluid can be formulated through the energy balance, including viscous dissipation. The dissipation energy is

$$E_v^* = \frac{16\pi}{\mathrm{Re}} \int_0^{t^*} R^* \dot{R}^{*2} \mathrm{d}t^*. \tag{21}$$

After accounting for this energy dissipation in the energy balance, the exact implicit equation for the bubble wall velocity becomes

$$\dot{R}^* = -\left[\frac{2}{3}\left(\frac{1}{R^{*3}}-1\right) - \frac{8}{\mathrm{Re}\,R^{*3}} \int_1^{R^*} R^* \dot{R}^* \,\mathrm{d}R^*\right]^{1/2}. \tag{22}$$

Then, the exact collapse time is

$$t_c^* = \int_1^0 \frac{1}{\dot{R}^*}\mathrm{d}R^* = \int_1^0 -\left[\frac{2}{3}\left(\frac{1}{R^{*3}}-1\right) - \frac{8}{\mathrm{Re}\,R^{*3}} \int_1^{R^*} R^* \dot{R}^* \,\mathrm{d}R^*\right]^{-1/2} \mathrm{d}R^*. \tag{23}$$

Substituting (12) and (20) into the left-hand side of (11) and (23) into the right-hand side, we evaluate the nested integral to obtain an implicit relationship for $\mathcal{C}(\mathrm{Re})$ as,

$$t_{\mathrm{RC}}^*\left(1 - \frac{4\mathcal{C}}{2\mathcal{C}+\sqrt{\mathrm{Re}^2 t_{\mathrm{RC}}^{*2}+4\mathcal{C}^2}}\right)^{-1/2} = -\sqrt{\frac{3}{2}} \int_1^0 \left(-1 + \frac{1}{R^{*3}} - \frac{4\sqrt{6}}{\mathrm{Re}\,\Gamma\left[\frac{5}{3}\right] R^{*3}}\left(1\right.\right.$$
$$\left.\left. - \frac{4\mathcal{C}}{2\mathcal{C}+\sqrt{\mathrm{Re}^2 t_{\mathrm{RC}}^{*2}+4\mathcal{C}^2}}\right)^{1/2}\left[\sqrt{\pi}\,\Gamma\left[\frac{7}{6}\right] - 2\sqrt{R^*}\,\Gamma\left[\frac{5}{3}\right]\,{}_2F_1\left(-\frac{1}{2},\frac{1}{6};\frac{7}{6};R^{*3}\right)\right]\right)^{-1/2}\mathrm{d}R^*, \tag{24}$$

where ${}_2F_1$ is Gauss's hyper-geometric function. The right-hand side can be numerically integrated to find the value of $\mathcal{C}$ for a given Reynolds number. For a fast calculation, we approximate the implicit function with a perturbation series where the small parameter is $1/\mathrm{Re}$ such that $\mathcal{C} \approx \mathcal{C}_0 + \mathcal{C}_1/\mathrm{Re} + \mathcal{C}_2/\mathrm{Re}^2 + \mathcal{O}(1/\mathrm{Re}^3)$. Constants $\mathcal{C}_0$, $\mathcal{C}_1$, and $\mathcal{C}_2$ approximate the implicit function in (24) and are found by numerically integrating and iterating for three separate Reynolds numbers. The following values that approximate (24) are $\mathcal{C}_0 = 0.46379$, $\mathcal{C}_1 = 0.56391$, and $\mathcal{C}_2 = 5.74916$.

2.3.3. Kelvin–Voigt viscoelasticity

The total Kelvin–Voigt stress integral average is the sum of the individual averages of the viscous and elastic contributions,

$$\overline{f}^*_{\mathrm{KV}} = \overline{f}^*_{\mathrm{v}} + \overline{f}^*_{\mathrm{NH}} = \frac{4\mathcal{C}}{2\mathcal{C} + \sqrt{\mathrm{Re}^2 t^{*2}_{\mathrm{RC}} + 4\mathcal{C}^2}} + \frac{1}{\mathrm{Ca}} \left(\sqrt{\frac{2}{3}} \frac{R^*_0 \pi}{t_{\mathrm{RC}}} - \frac{5}{2} \right). \tag{25}$$

2.3.4. Maxwell viscoelasticity

The stress integral for the Maxwell model has no closed-form relationship. We approximate the right-hand side of the stress integral ODE in table 2 to be $\overline{f}^*_{\mathrm{v}}$ and obtain the approximate relationship for the stress integral

$$S^*_{\mathrm{m}} = f^*_{\mathrm{m}} \approx \overline{f}^*_{\mathrm{v}} - \left(\overline{f}^*_{\mathrm{v}} - f^*_{\mathrm{m,o}} \right) \exp\left[-\frac{t^*}{\mathrm{De}} \right], \tag{26}$$

where $f^*_{\mathrm{m,o}}$ is the non-relaxed stress in the surrounding material at the maximum radius due to the expansion. For $\mathrm{De} \ll 1$, $f^*_{\mathrm{m,o}} \approx 0$. When this condition is not satisfied, the initial stress can substantially alter the subsequent bubble dynamics. The initial stress due to the expansion within a Maxwell fluid has no closed form, as such it is found numerically. Taking the integral average,

$$\overline{f}^*_{\mathrm{m}} = \overline{f}^*_{\mathrm{v}} + \frac{\mathrm{De}}{t^*_c} \left(\left(\overline{f}^*_{\mathrm{v}} - f^*_{\mathrm{m,o}} \right) \exp\left[-\frac{t^*_c}{\mathrm{De}} \right] - \overline{f}^*_{\mathrm{v}} + f^*_{\mathrm{m,o}} \right), \tag{27}$$

we can obtain an implicit relationship for $\overline{f}^*_{\mathrm{m}}$ by substituting (12) into the previous expression. However, this relationship has no analytical solution for $\overline{f}^*_{\mathrm{m}}$ because t^*_c is the actual collapse time that depends on $\overline{f}^*_{\mathrm{m}}$. For small initial stress, $f^*_{\mathrm{m,o}}$, $\overline{f}^*_{\mathrm{m}}$ is maximized when $\mathrm{De} \to 0$ corresponding to the viscous solution. Because the modification function is bounded by the viscous solution, which, for relevant parameters, has a small effect on the collapse time, we approximate the remaining collapse time dependence, t^*_c, by the Rayleigh collapse time,

$$\overline{f}^*_{\mathrm{m}} = \overline{f}^*_{\mathrm{v}} + \frac{\mathrm{De}}{t^*_c} \left(\left(\overline{f}^*_{\mathrm{v}} - f^*_{\mathrm{m,o}} \right) \exp\left[-\frac{t^*_{\mathrm{RC}}}{\mathrm{De}} \right] - \overline{f}^*_{\mathrm{v}} + f^*_{\mathrm{m,o}} \right). \tag{28}$$

2.3.5. Standard linear solid using neo-Hookean elasticity

We consider a material model comprising a Maxwell element parallel to a neo-Hookean elastic element. Since the deviatoric Cauchy stress tensor is a sum of contributions, the stress integral is summed as $S^*_{\mathrm{SLS}} = S^*_{\mathrm{m}} + S^*_{\mathrm{NH}}$ and $\dot{S}^*_{\mathrm{SLS}} = \dot{S}^*_{\mathrm{m}} + \dot{S}^*_{\mathrm{NH}}$. Therefore, one obtains the stress integral relationship found in table 2. Additionally, the collapse time modification factor is a sum of the individual factors, $\overline{f}^*_{\mathrm{SLS}} = \overline{f}^*_{\mathrm{m}} + \overline{f}^*_{\mathrm{NH}}$ since the mean value is a linear operator.

2.4. Experimental methods

The laser microcavitation experiments follow the general LIC procedure of Estrada et al. [14], with two main advancements of shadowgraph and ghost imaging and incident beam shaping [32], as shown in fig. 1. These are described in more detail in Appendix B and summarized here.

Single LIC bubble events are generated in soft hydrogels using a pulsed, frequency-doubled (532 nm), Q-switched Nd:YAG laser. The pulse energy is user-defined and was on the order of $1-10\,\mathrm{mJ}$ for the experiments herein. A diffraction-limited focusing objective condenses the laser pulse into a
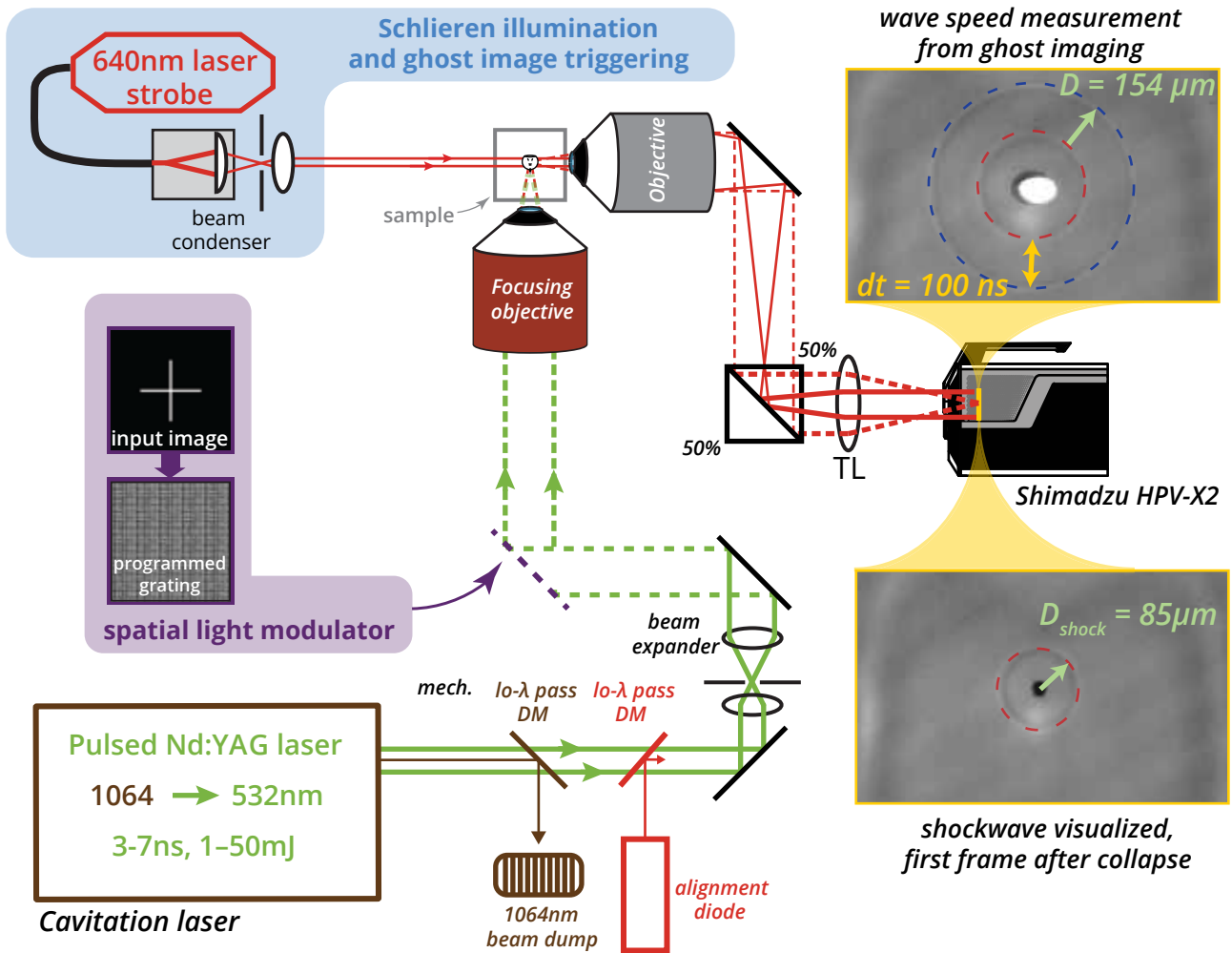
Figure 1: The experimental setup to generate, record, and profile single laser-induced microcavitation (LIC) bubble events in soft materials. The setup uses a combination of a class-4, frequency-doubled Q-switched 532 nm Nd:YAG pulsed laser, a high-speed imaging camera, and a spatial light modulator. The time of the first bubble collapse is estimated according to the shock wave, which was visualized by shadowgraph and ghost imaging techniques.

beam waist to approximately $4\,\mu\text{m}$ in diameter. A second objective is oriented orthogonal to the imaging plane for the purpose of verifying bubble sphericity. A spatial light modulator is used to tune higher-order beam asymmetry to create spherical bubble events. We record the microcavitation event at 1 million frames per second (Mfps) using a Shimadzu HPV-X2 (Tokyo, Japan) ultra-high-speed imaging camera. A backlight laser strobe fires synchronously with the camera and is sent to the bubble event as parallel light. This light enables shadowgraph imaging, a mode related to Schlieren imaging that permits the visualization and measurement of emitted shockwaves. We strobe the shadowgraph backlight twice per frame, improving our estimate of the collapse time using the shock speed (found by locating two shocks on one frame) and the minimum radius estimate.

Polyacrylamide gels for characterization purposes were prepared at concentrations of 5%/0.03% and 10%/0.06% acrylamide/bisacrylamide (v/v) according to previously developed protocols [33] and our prior work [14]. The polyacrylamide gels were cast in square $5\,\text{mL}$ polystyrene spectrophotometer cuvettes and cured for $45\,\text{min}$ prior to characterization.

Viscous liquid samples were produced by mixing PEGDA of molecular weight 8,000 with distilled water in a proportion of 80% PEGDA by volume. The blended mixtures were poured into glass-bottomed, $35\,\text{mm}$ diameter Petri dishes up to roughly $2\,\text{mm}$ of depth. These prepared samples retained a liquid state with no signs of heterogeneity. The low-frequency shear moduli of the PEGDA samples were measured using a TA Instrument ARES-G2 rotational rheometer (New Castle, DE) equipped with a $40\,\text{mm}$ diameter stainless steel $2°$-angle cone plate fixture and a flat base. Dynamic loading was applied at a frequency of $1\,\text{rad/s}$ with the maximum strain amplitude of $0.04\,\text{rad}$.

2.5. Parsimonious inverse characterization based on bubble collapse time

Past studies using IMR have found that adjusting the laser energy can modulate the maximum radius of the bubble. The amplification factor of the initial bubble expansion, $\Lambda_{\max} = R_{\max}/R_0$, is weakly sensitivity to laser energy [34]. Following this approach, we can perform LIC experiments at various laser energy levels on a common material and tune the parameters appearing in the non-dimensional Keller–Miksis equation. In the context of the energy balance analysis, our experiments traverse the $\{R_{\max}, \Lambda_{\max}\}$ space for a constant set of dimensional viscoelastic parameters, as illustrated in fig. 2 for a Kelvin–Voigt model, and collect $t_{\text{c}}^*(R_{\max}, \Lambda_{\max})$.

We solve for the viscoelastic model parameters that minimize the difference between the collapse times that were analytically estimated and those that were experimentally measured. We refer to this new inverse characterization method as the parsimonious Inertial Microcavitation Rheometry technique (pIMR).

To quantify the accuracy of the pIMR, we define the fitting error for a material parameter q as,

$$\epsilon_q = |\log_2\left(q^{\text{pIMR}}/q^{\text{IMR}}\right)|, \tag{29}$$

where q^{pIMR} is the solution obtained with the proposed pIMR procedure and q^{IMR} is the solution obtained with the IMR procedure based on forward simulations of the full-physics model. For example, $\epsilon_q = 1$ would mean that the inversely estimated q either underestimated or overestimated Ca by a multiplicative factor of 2.

Ideally, the pIMR would match the accuracy of the full IMR procedure for estimating viscoelastic parameters—i.e., ϵ_G, ϵ_μ, $\epsilon_{\tau_1} \to 0$. However, our goal in the present work is for the pIMR to substitute a coarse-scale sweep of the parameter space. Using the IMR, this sweep is equivalent to defining a realistic range of viscoelastic parameters (e.g., $G \in [1, 10^3]$ kPa and $\mu \in [10^{-3}, 1]$ Pa · s for the Kelvin–Voigt representation of a typical hydrogel) and simulating the dynamics of trial parameters.
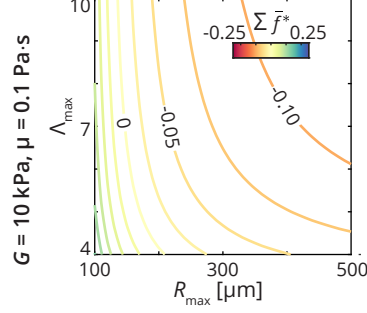
Figure 2: Combined effect of viscoelasticity, bubble pressure, surface tension, and compressibility for bubble collapse in a Kelvin–Voigt material with $\{G = 10\,\mathrm{kPa}, \mu = 0.1\,\mathrm{Pa}\cdot\mathrm{s}\}$ across typical range of $R_{\max}$ and $\Lambda_{\max}$ in IMR.

Comparing the simulated and experimentally measured bubble dynamics within a period of interest identifies a parametric range for a secondary, fine-scale sweep.

In practice, the choice of an acceptable error depends on the user's problem of interest. For illustrative purposes, we demand herein that the pIMR estimates the material moduli G and μ each to within a range of $2/3$ to $3/2$ times of the reference solution found through the IMR procedure. This relative error corresponds to values of $\epsilon_G, \epsilon_\mu \leqslant 0.6$. For the Kelvin–Voigt model, this is equivalent to the accuracy achieved over a brute-force sweep over 256 sets of $\{G, \mu\}$ or approximately an hour of computational time. For τ_1 in Maxwell-type stress response, we aim for the pIMR solution to be within an order of magnitude of the reference IMR solution, which corresponds to $\epsilon_{\tau_1} \leqslant 3.3$.

3. Verification of approximated collapse times

To verify the approximated collapse time as a reliable substitute for the full-physics bubble dynamics model for inversely characterizing material viscoelasticity, we introduce an error measure $\phi\left(R_{\max}, \Lambda_{\max}, \mathrm{Ca}, \mathrm{Re}, \mathrm{De}\right)$ to quantify the agreement of the two theoretical frameworks in predicting the bubble collapse time:

$$
\begin{aligned}
\phi &= \log_{10}\left| \left(\frac{t_{\mathrm{RC}}^*}{t_{\mathrm{c}}^{*,\mathrm{EB}}\left(R_{\max}, \Lambda_{\max}, \mathrm{Ca}, \mathrm{Re}, \mathrm{De}\right)}\right)^2 - \left(\frac{t_{\mathrm{RC}}^*}{t_{\mathrm{c}}^{*,\mathrm{FP}}\left(R_{\max}, \Lambda_{\max}, \mathrm{Ca}, \mathrm{Re}, \mathrm{De}\right)}\right)^2 \right| \\
&= \log_{10}\left| \overline{f}^*\left(R_{\max}, \Lambda_{\max}, \mathrm{Ca}, \mathrm{Re}, \mathrm{De}\right) - \left[1 - \left(\frac{t_{\mathrm{RC}}^*}{t_{\mathrm{c}}^{*,\mathrm{FP}}\left(R_{\max}, \Lambda_{\max}, \mathrm{Ca}, \mathrm{Re}, \mathrm{De}\right)}\right)^2\right] \right|.
\end{aligned}
\tag{30}
$$

Here, $t_{\mathrm{c}}^{*,\mathrm{FP}}$ is the collapse time calculated by the full-physics bubble dynamics model, and $t_{\mathrm{c}}^{*,\mathrm{EB}}$ is the approximate collapse time calculated by the energy balance analysis. We treating the collapse time calculated in the full-physics model as a reference. The error indicates the order of difference between the approximation and full-physics approaches in describing the combined effect of the contributing physics. For our analysis of ϕ, we approximate the errors $\{\epsilon_G, \epsilon_\mu, \epsilon_{\tau_1}\}$ considered during the inverse characterization of the viscoelastic model parameters.

We begin by examining the bubble collapse time in the absence of material viscoelasticity when an inviscid, nearly incompressible material surrounds the gas-containing bubble. The resulting $\overline{f}^*$ is as shown in fig. 3 (a) for the typical range of $R_{\max}$ and $\Lambda_{\max}$ relevant to our LIC experiments. Figure 3 (b) shows the corresponding error ϕ, with a maximum value of -1.9 in the range of

13
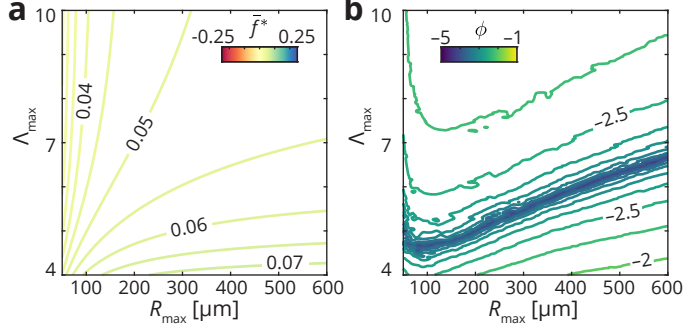
Figure 3: Bubble collapse in inviscid material: (a) combined effect of bubble pressure ($\overline{f}^*_{\mathrm{bc}}$), surface tension ($\overline{f}^*_{\mathrm{We}}$), and material compressibility ($\overline{f}^*_{\mathrm{wc}}$); and (b) error function ϕ, comparing approximate bubble collapse time and full-physics calculation.

$\{R_{\max}, \Lambda_{\max}\}$ relevant to our LIC experiments. Relative to the full-physics model calculation, the energy balance approximation underestimates the bubble collapse time for $\Lambda_{\max} \lesssim 5$ and overestimates the bubble collapse time for $\Lambda_{\max} \gtrsim 6$. The sensitivity of ϕ to $\Lambda_{\max}$ suggests that the discrepancy between the two models mainly arises from the effect of the bubble pressure. As noted in Section 2.2.2, the collapse time modification function $\overline{f}^*_{\mathrm{bc}}$ represents the $\Lambda_{\max}$-dependence of the collapse time in a bubble surrounded by an inviscid material. However, this function does not fully capture the effect of the spatially non-uniform temperature and vapor concentration considered in the full-physics model.

For a neo-Hookean hyperelastic material, the effect of stress on collapse time, $\overline{f}^*_S(\mathrm{Ca})$ is shown in fig. 4 (a). As $\Lambda_{\max}$ increases at a fixed Cauchy number, the magnitude of $\overline{f}^*_S$ increases. The resulting error ϕ is shown in fig. 4 (b) for the representative case of $R_{\max} = 100$ μm, with $\phi < -1.4$ when Ca > 5. For a Newtonian viscous material, $\overline{f}^*_S(\mathrm{Re})$ is shown in fig. 4 (c). For the highlighted case of $R_{\max} = 100\,\mathrm{μm}$, ϕ is shown in fig. 4 (d), with $\phi < -1.7$. A low Reynolds number ($\lesssim 5$) results in overdamped bubble dynamics, for which a collapse time is no longer defined.

Combining the neo-Hookean and Newtonian effects, we obtain $\overline{f}^*_S(\mathrm{Ca}, \mathrm{Re})$ in a Kelvin–Voigt material, presented in fig. 5 (a) and (c) for the representative cases of $\Lambda_{\max} = 5$ and 9. Figure 5 (b) and (d) show that $\phi < -1.2$ for the highlighted scales of $\Lambda_{\max}$ at $R_{\max} = 100\,\mathrm{μm}$. The resulting $\overline{f}^*_S$ is larger in magnitude compared to the contribution of non-viscoelastic physics shown in fig. 3. This result confirms that viscoelasticity is the primary contributor to bubble collapse in LIC experiments and attests to the validity of inverse characterization of viscoelasticity based on the collapse time.

From the landscape of ϕ calculated, we can estimate the order of error anticipated during the inverse calculation of $\{\mathrm{Ca}, \mathrm{Re}\}$. Given a fixed set of $\{R_{\max}, \Lambda_{\max}\}$, we find $\widetilde{\mathrm{Ca}}(\mathrm{Ca}, \mathrm{Re})$ satisfying $t_{\mathrm{c}}^{*,\mathrm{EB}}(\widetilde{\mathrm{Ca}}, \mathrm{Re}) = t_{\mathrm{c}}^{*,\mathrm{FP}}(\mathrm{Ca}, \mathrm{Re})$, and an approximate error $\tilde{\epsilon}_{\mathrm{Ca}} = |\log_2(\widetilde{\mathrm{Ca}}/\mathrm{Ca})|$. The quantity $\widetilde{\mathrm{Ca}}$ is an adjusted Cauchy number that resolves the disagreement between the approximate collapse time and the full-physics calculation of collapse time, while Re, $R_{\max}$, and $\Lambda_{\max}$ remain unchanged. In other words, we conservatively ascribe all disagreement between the approximation and full-physics approaches to $\widetilde{\mathrm{Ca}}$ and determine the possible error in the prediction of Ca. For the case of $R_{\max} = 100\,\mathrm{μm}$ and $\Lambda_{\max} = 5$, $\tilde{\epsilon}_{\mathrm{Ca}}(\mathrm{Ca}, \mathrm{Re})$ is plotted in fig. 6 (a). When either Ca < 20 or Re > 7, we have $\tilde{\epsilon}_{\mathrm{Ca}} < 0.6$, corresponding to a tolerable multiplicative error factor below 1.5. The region of higher $\tilde{\epsilon}_{\mathrm{Ca}}$ shown in fig. 6 (a) corresponds to combinations of $\{\mathrm{Ca}, \mathrm{Re}\}$ in which the neo-Hookean elasticity contributes weakly to the bubble collapse, as illustrated in fig. 5 (a). Similar to our definition of $\widetilde{\mathrm{Ca}}$, we find $\widetilde{\mathrm{Re}}(\mathrm{Ca}, \mathrm{Re})$ satisfying $t_{\mathrm{c}}^{*,\mathrm{EB}}(\mathrm{Ca}, \widetilde{\mathrm{Re}}) = t_{\mathrm{c}}^{*,\mathrm{FP}}(\mathrm{Ca}, \mathrm{Re})$, with the corresponding error

14
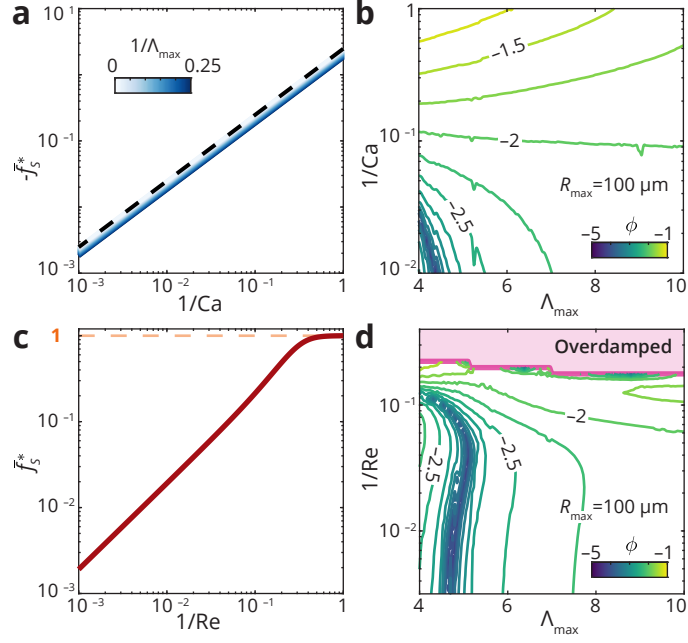
Figure 4: Bubble collapse in single-parameter constitutive models. Neo-Hookean hyperelasticity: (a) effect of the stress on collapse time, $\overline{f}_S^*[\mathrm{Ca}]$; (b) error ϕ for $R_{\max} = 100\,\mu\mathrm{m}$. Newtonian viscosity: (c) effect of the stress on collapse time, $\overline{f}_S^*[\mathrm{Re}]$, which converges to 1 as $\mathrm{Re} \to 0$; (d) error ϕ for $R_{\max} = 100\,\mu\mathrm{m}$. For $\mathrm{Re} \lesssim 5$, the full-physics model predicts overdamped bubble dynamics, with R^* gradually relaxing toward its equilibrium value R_0^*, rather than violently collapsing and oscillating about R_0^*.
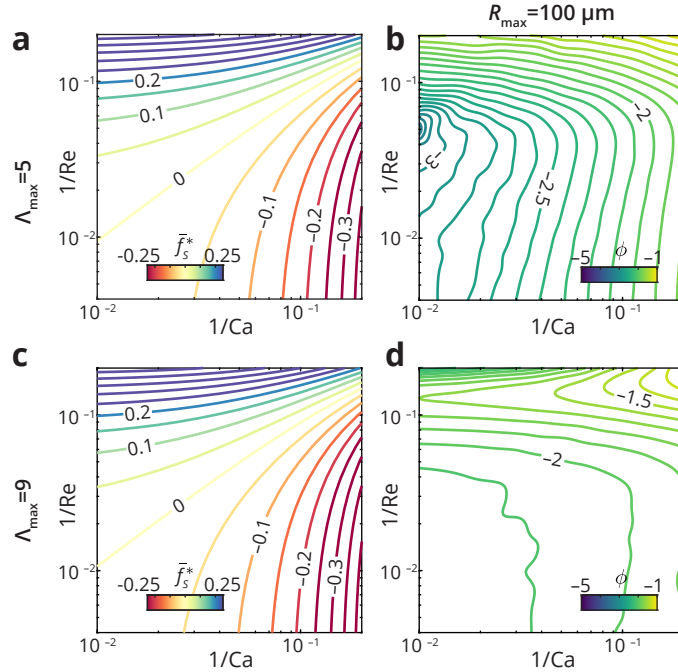
Figure 5: Bubble collapse in Kelvin–Voigt viscoelastic material. $\Lambda_{\max} = 5$: (a) effect of viscoelasticity, $\overline{f}_S^*[\mathrm{Ca}, \mathrm{Re}]$, as estimated by the energy balance analysis, and (b) error function ϕ for $R_{\max} = 100$ µm; $\Lambda_{\max} = 9$: (c) effect of viscoelasticity, $\overline{f}_S^*[\mathrm{Ca}, \mathrm{Re}]$, as estimated by the energy balance analysis, and (d) error function ϕ for $R_{\max} = 100$ µm.

15
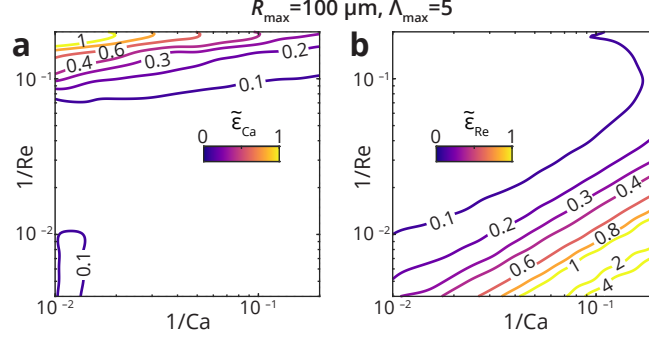
Figure 6: Approximated error in inversely characterized Kelvin–Voigt model parameters for $R_{\mathrm{max}} = 100\,\mu\mathrm{m}$ and $\Lambda_{\mathrm{max}} = 5$: (a) Cauchy number (Ca), (b) Reynolds number (Re).

$\tilde{\epsilon}_{\mathrm{Re}} = |\log_2(\widetilde{\mathrm{Re}}/\mathrm{Re})|$ plotted in fig. 6 (b) for the case of $R_{\mathrm{max}} = 100\,\mu\mathrm{m}$ and $\Lambda_{\mathrm{max}} = 5$. When either $\mathrm{Re} < 60$ or $\mathrm{Ca} > 40$, $\tilde{\epsilon}_{\mathrm{Re}} < 0.6$. The region of higher $\tilde{\epsilon}_{\mathrm{Re}}$ corresponds to combinations of $\{\mathrm{Ca}, \mathrm{Re}\}$ in which the viscosity contribution to the bubble collapse, $\overline{f}_{\mathrm{v}}^{*}$, is less than the elasticity contribution, $\overline{f}_{\mathrm{NH}}^{*}$, by an order of magnitude or more. The broadly low values of $\tilde{\epsilon}_{\mathrm{Ca}}$ and $\tilde{\epsilon}_{\mathrm{Re}}$ in fig. 6 suggest that the approximated collapse time can accurately recover Ca and Re.

For a Maxwell material, $\overline{f}_{S}^{*}(\mathrm{Re}, \mathrm{De})$ is shown in fig. 7 (a, b) for the cases of $\Lambda_{\mathrm{max}} = 5$ and 9. In fig. 7 (b), the gray-shaded region corresponds to combinations of $\{\mathrm{Re}, \mathrm{De}, \Lambda_{\mathrm{max}}\}$ that are unattainable with the initial growth simulation. The error ϕ, shown in fig. 7 (c, d) for the highlighted cases of $\{R_{\mathrm{max}}, \Lambda_{\mathrm{max}}\}$, is compounded by the errors in estimating the contribution of material viscosity to the collapse time and the added contribution of viscoelastic relaxation. The error ϕ increases with the stronger viscous effect at lower Re. The discrepancy between the energy balance and full-physics results is most pronounced for $0.1 \leqslant \mathrm{De} \leqslant 1$, in which case the relaxation time scale is comparable to the characteristic time scale of the bubble dynamics. When $\mathrm{Re} = 10$ and $\{R_{\mathrm{max}} = 100\,\mu\mathrm{m}, \Lambda_{\mathrm{max}} = 5\}$, ϕ increases from -1.8 at $\mathrm{De} = 10^{-2}$ to -0.9 at $\mathrm{De} = 0.3$ and then decreases again to -2.8 at $\mathrm{De} = 10$. The full-physics model predicts that a Maxwell model with a combination of low Re $(\lesssim 10)$ and low De $(\lesssim 1)$ leads to over-damped bubble dynamics without a finite collapse time, corresponding to the pink-shaded regions in fig. 7 (c, d).

Last, we examine the bubble collapse in an SLS material parameterized by Ca, Re, and De. The effect of viscoelastic stress, $\overline{f}_{S}^{*}$, is the sum of the neo-Hookean and Maxwell contributions shown earlier in fig. 4 (a) and fig. 7 (a). Figure 8 (a) and (b) show the error ϕ at fixed elasticity of $\mathrm{Ca} = 32$ and 3.2 for $\{R_{\mathrm{max}} = 100\,\mu\mathrm{m}, \Lambda_{\mathrm{max}} = 5\}$. When $\mathrm{Re} > 30$, we have $\phi < -1.2$, comparable to the error in the Maxwell model shown in fig. 7. When Re is further decreased, the strong viscous effect results in overdamped bubble dynamics and an increased ϕ, as seen previously in fig. 7 for the Maxwell model.

Similar to our earlier analysis for the Kelvin–Voigt model, we conservatively estimate the inverse fitting errors from the model mismatch reflected in ϕ in fig. 8. For the case of $R_{\mathrm{max}} = 100\,\mu\mathrm{m}$, $\Lambda_{\mathrm{max}} = 5$, and $\mathrm{Ca} = 32$ illustrated in fig. 8 (a), $\tilde{\epsilon}_{\mathrm{Ca}} = |\log_2(\widetilde{\mathrm{Ca}}/\mathrm{Ca})|$, $\tilde{\epsilon}_{\mathrm{Re}} = |\log_2(\widetilde{\mathrm{Re}}/\mathrm{Re})|$, and $\tilde{\epsilon}_{\mathrm{De}} = |\log_2(\widetilde{\mathrm{De}}/\mathrm{De})|$ are plotted in fig. 9. From fig. 9 (a), we observe that $\tilde{\epsilon}_{\mathrm{Ca}} > 0.6$ in the region with $\phi > -1.5$ in fig. 8 (a), where Re is low and the Maxwell branch has a stronger contribution to the bubble collapse than the ground-state elasticity. We see in fig. 9 (b) and (c) that $\tilde{\epsilon}_{\mathrm{Re}} > 0.6$ and $\tilde{\epsilon}_{\mathrm{De}} > 3$ when $\mathrm{De} \gtrsim 0.1$ and $\mathrm{Re} \gtrsim 30$, corresponding to a weak contribution of the Maxwell branch to the bubble collapse. Otherwise, the conservatively estimated fitting errors suggest that the SLS model parameters $\{\mathrm{Ca}, \mathrm{Re}, \mathrm{De}\}$ can be inversely characterized to an acceptable accuracy when the
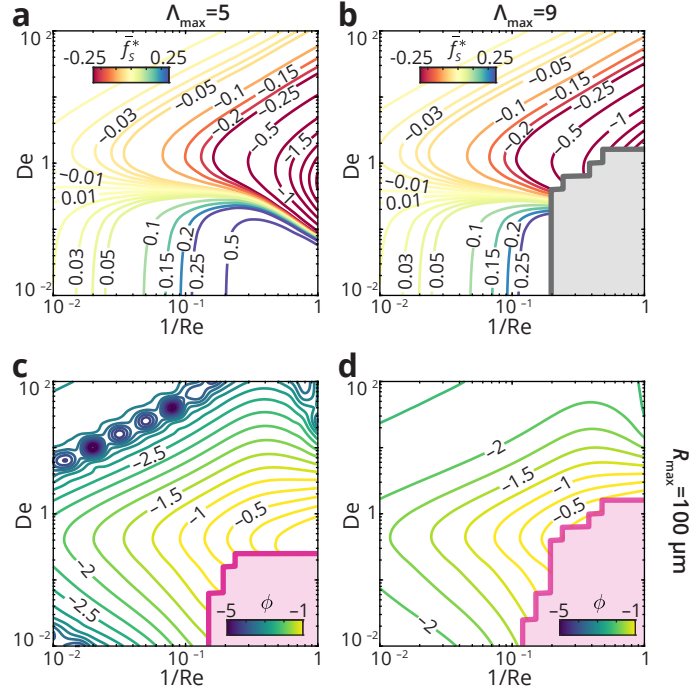
Figure 7: Bubble collapse in Maxwell material: effect of viscoelasticity ($\overline{f}_S^*[\mathrm{Re}, \mathrm{De}]$), as estimated by the energy balance analysis, for (a) $\Lambda_{\max} = 5$ and (b) $\Lambda_{\max} = 9$; error function ϕ for (c) $R_{\max} = 100\,\mu\mathrm{m}$ and $\Lambda_{\max} = 5$, and (d) $R_{\max} = 100\,\mu\mathrm{m}$ and $\Lambda_{\max} = 9$. In the gray region, the required amplification factor $\Lambda_{\max}$ is unattainable during the bubble growth. In the pink regions, the full-physics model predicts overdamped bubble dynamics without a finite collapse time.
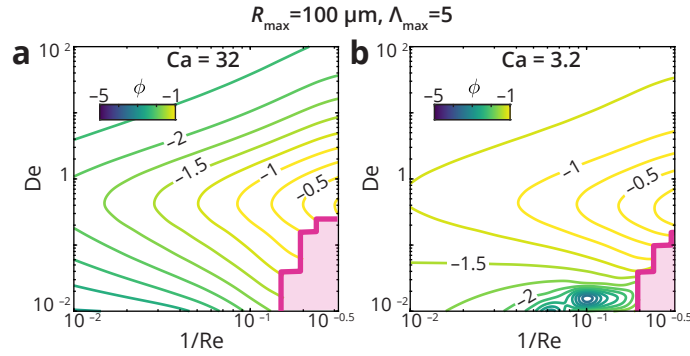
Figure 8: Bubble collapse in SLS material, with $R_{\max} = 100$ µm and $\Lambda_{\max} = 5$: error function ϕ for (a) Ca = 32 and (b) Ca = 3.2. In the pink regions, the full-physics model predicts overdamped bubble dynamics without a finite collapse time.
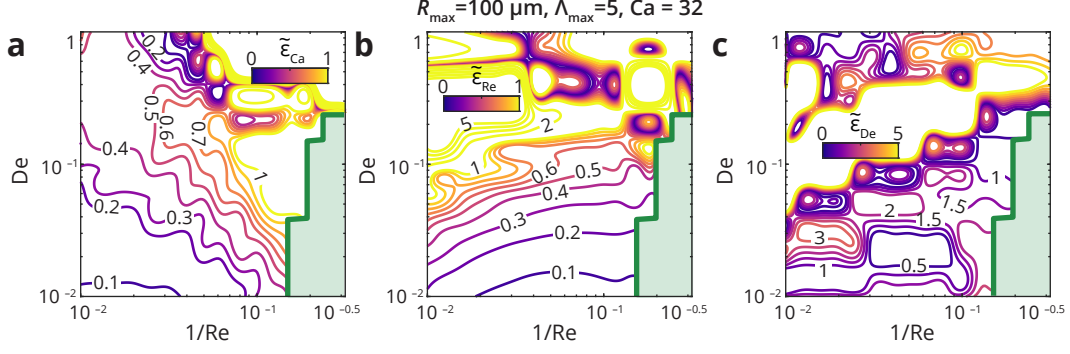
Figure 9: Approximated error in inversely characterized SLS model parameters for $R_{\max} = 100\,\mu\text{m}$, $\Lambda_{\max} = 5$: (a) Cauchy number, (b) Reynolds number, (c) Deborah number. The green region is equivalent to the pink regions shown in Figure 8(a), where the full-physics model predicts overdamped bubble dynamics without a finite collapse time.

corresponding collapse time modification factors are not negligible—i.e., $|\overline{f}^*_{\text{NH}}|\,|\overline{f}^*_{\text{m}}| \gtrsim 0.1$.

4. Inverse characterization of viscoelastic materials

In this section, we apply the proposed pIMR procedure to the inverse characterization of viscoelastic materials from typical LIC experiment results. To facilitate the inverse characterization process, we construct a cost function,

$$\psi\left[G, \mu, \tau_1\right] = \log_{10}\left[\frac{1}{n}\sum_{k=1}^{n}\left(\left(\frac{t_{\text{c}}^{\text{Expt}}\left[R_{\max,k}, \Lambda_{\max,k}\right]}{t_{\text{c}}^{\text{EB}}\left[G, \mu, \tau_1, R_{\max,k}, \Lambda_{\max,k}\right]}\right)^2 - 1\right)^2\right], \tag{31}$$

that quantifies the agreement between the collapse time measured experimentally, $t_{\text{c}}^{\text{Expt}}$, and the predicted value, t_{c}^{EB}, for a set of trial parameters, $\{G, \mu, \tau_1\}$ according to the energy balance analysis. The cost function can be interpreted as the order of mean square relative error between the measured and predicted collapse time. With a Nelder–Mead direct search process [35], an optimal set of viscoelastic parameters is then determined to minimize ψ. In contrast to prior work [14], this approach enables the use of data from multiple experiments to arrive at a batch-fit solution.

To analyze the precision of the inverse characterization solution, we also introduce the normalized cost function for experimental data, $\hat{\psi}[G, \mu, \tau_1] = \psi[G, \mu, \tau_1] - \psi_0$, where ψ_0 is the cost function corresponding to the optimal solution found by the direct search algorithm. The normalized cost $\hat{\psi}$ is equal to zero at the optimal solution, while the positive-valued $\hat{\psi}$ elsewhere reflects how far the solution is from being optimal.

4.1. Recovery of viscoelastic material parameters from synthetic experiments

As a primary verification of pIMR, we use it to recover the viscoelastic model parameters from synthetic experiments. Using the full-physics model, we simulated bubble dynamics histories $R(t)$ for a fixed set of Kelvin–Voigt model parameters $\{G = 10\,\text{kPa}, \mu = 0.10\,\text{Pa·s}\}$ with 36 different pairs of $R_{\max} \in [100, 400]$ μm and $\Lambda_{\max} \in [5, 9]$. The bubble geometry parameters, as shown in fig. 10 (a), were generated with the Latin hypercube sampling method [36], assuming that both $R_{\max}$ and $\Lambda_{\max}$ are uniformly distributed.

18

Using all $n = 36$ samples, the optimized Kelvin–Voigt parameters are $\{G = 10.11\,\text{kPa}, \mu = 0.0945\,\text{Pa}\cdot$ s, corresponding to errors of $\epsilon_G = 0.016$ and $\epsilon_\mu = 0.082$. The normalized cost function space, shown in fig. 10 (b), indicates good precision. The region of $\hat{\psi} \leqslant 1$ spans a narrow range of $G \in (9.4, 10.8)$ kPa, $\mu \in (0.084, 0.099)$ Pa·s, with upper-to-lower bound ratio of 1.15 and 1.18. The bubble dynamics corresponding to the optimized solution is simulated with the full-physics model for one of the synthetic experiments and matches well with the input $R(t)$, as shown in fig. 10 (e).

When a subset of $n = 9$ samples is used, we obtain $\epsilon_G = 0.016$ and $\epsilon_\mu = 0.082$ and the normalized cost function space shown in fig. 10 (c), similar to that of the $n = 36$ case. For the extreme case of $n = 2$, we obtain solutions with $\epsilon_G = 0.010$ and $\epsilon_\mu = 0.138$. Though fig. 10 (d) exhibits increased precision for the $n = 2$ solution compared to the higher n cases, the decreased accuracy with lower n suggests an increased sensitivity to the minor disagreements between the full-physics and approximated collapse times. If we systematically add a relative error of 1% to the collapse time in the synthetic experiment data, the resulting errors for $n = 36, 9$, and 2 are $\{\epsilon_G = 0.149, \epsilon_\mu = 0.092\}$, $\{\epsilon_G = 0.149, \epsilon_\mu = 0.088\}$, and $\{\epsilon_G = 0.191, \epsilon_\mu = 0.171\}$. The loss of accuracy due to the artificially introduced errors is more evident in the $n = 2$ case, indicating that an overly small sample size may make the measured collapse time more susceptible to errors.

Using the same $n = 36$ pairs of $R_{\max}$ and $\Lambda_{\max}$ from the previous example, we synthetically generate $R(t)$ for an SLS model with $\{G = 10\,\text{kPa}, \mu = 0.1\,\text{Pa}\cdot\text{s}, \tau_1 = 1\,\text{µs}\}$ and inversely characterized the SLS parameters with pIMR. The optimized solution is $\{G = 9.78\,\text{kPa}, \mu = 0.079\,\text{Pa}\cdot\text{s}, \tau_1 = 1.66\,\text{µs}\}$, with errors $\epsilon_G = 0.032$, $\epsilon_\mu = 0.340$, and $\epsilon_{\tau_1} = 0.731$. The resulting normalized cost function space is illustrated in fig. 11 (a). With the other parameters fixed to the pIMR solution, the range of $\hat{\psi}[G] \leqslant 1$ spanned 9.59–9.97 kPa, with an upper-to-lower bound ratio of 1.04. The corresponding range for $\hat{\psi}[\mu] \leqslant 1$ and $\hat{\psi}[\tau_1] \leqslant 1$ have upper-to-lower bound ratios of 1.12 and 1.45.

Using a Kelvin–Voigt model, optimal parameters of $\{G = 9.17\,\text{kPa}, \mu = 0.052\,\text{Pa}\cdot\text{s}\}$ are obtained from the SLS synthetic experiments. The bubble dynamics corresponding to optimized Kelvin–Voigt and SLS solutions are simulated for a representative synthetic experiment and compared with the input $R(t)$ in fig. 11 (c). Both the Kelvin–Voigt and SLS solutions accurately reproduced bubble collapse, with errors of 45 ns (0.15%) and 164 ns (0.56%) for the collapse time.

### 4.2. Characterization of water-PEGDA mixture (viscous fluid)

Next, we used pIMR to characterize uncured mixtures of water and PEGDA, which are expected to exhibit viscous fluid behavior with negligible elasticity. Figure 12 shows the characterization results for specimens with an 80% v/v PEGDA concentration.

A total of 18 LIC experiments were performed, with $R_{\max}$ ranging from 182.6 to 342.9 µm and $\Lambda_{\max}$ ranging from 4.73 to 5.33. The inverse fitting of the Kelvin–Voigt model using pIMR resulted in $G \approx 0$ and $\mu = 0.280\,\text{Pa}\cdot\text{s}$, converging to a Newtonian model. The optimized SLS parameters were determined to be $G \approx 0$, $\mu = 0.416\,\text{Pa}\cdot\text{s}$, and $\tau_1 = 4.43\,\text{µs}$, converging to a Maxwell model, with the $\hat{\psi}$ space shown in fig. 12 (b). In both the Kelvin–Voigt and SLS fitting processes, pIMR identifies the material as a fluid. The minimized ψ decreases from -1.61 to -2.63 and -2.91 as the constitutive model is advanced from the inviscid case to the Newtonian and Maxwell cases. In fig. 12 (a), the approximated collapse time t_c^{EB} for the optimized models is plotted versus the measured collapse time t_c^{Expt} of each experiment. We observe that t_c^{Expt} is larger than the predicted value for an inviscid material, confirming the dominance of material viscosity over elasticity during the bubble collapse.

From oscillatory shear plate rheometry testing, the low-frequency viscosity of the PEGDA-water
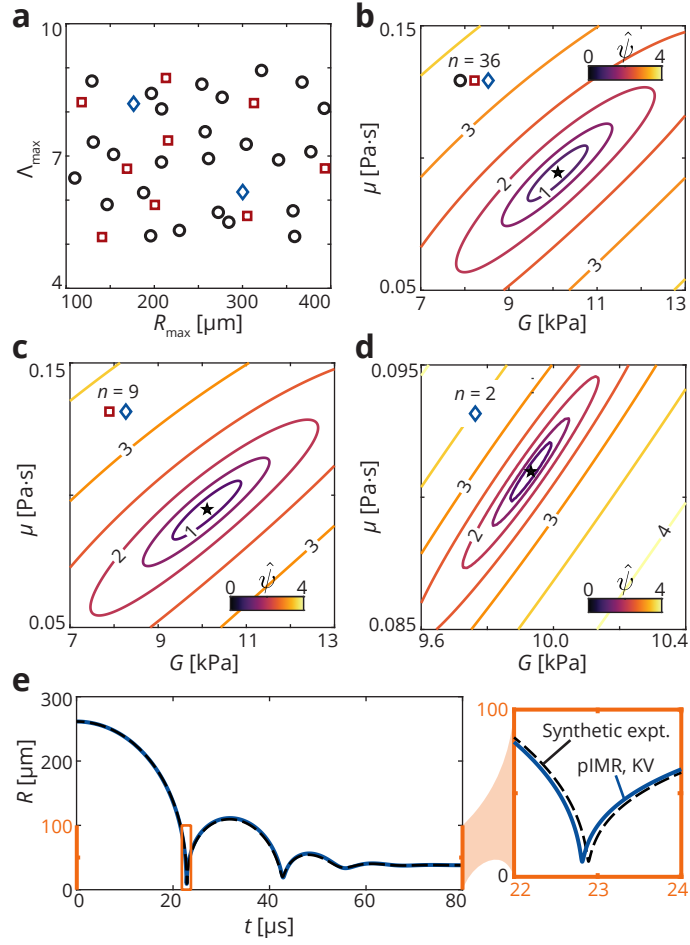
Figure 10: Recovery of viscoelastic model parameters from synthetic experiments of Kelvin–Voigt material. (a) Distribution of $\{R_{\max}, \Lambda_{\max}\}$ in synthetic data; cost function ψ space for sample sizes of (b) $n = 36$ (all points), (c) $n = 9$ ($\lozenge$ and $\square$), and (d) $n = 2$ ($\lozenge$); (e) typical bubble dynamics corresponding to the input parameters and the $n = 36$ solution.
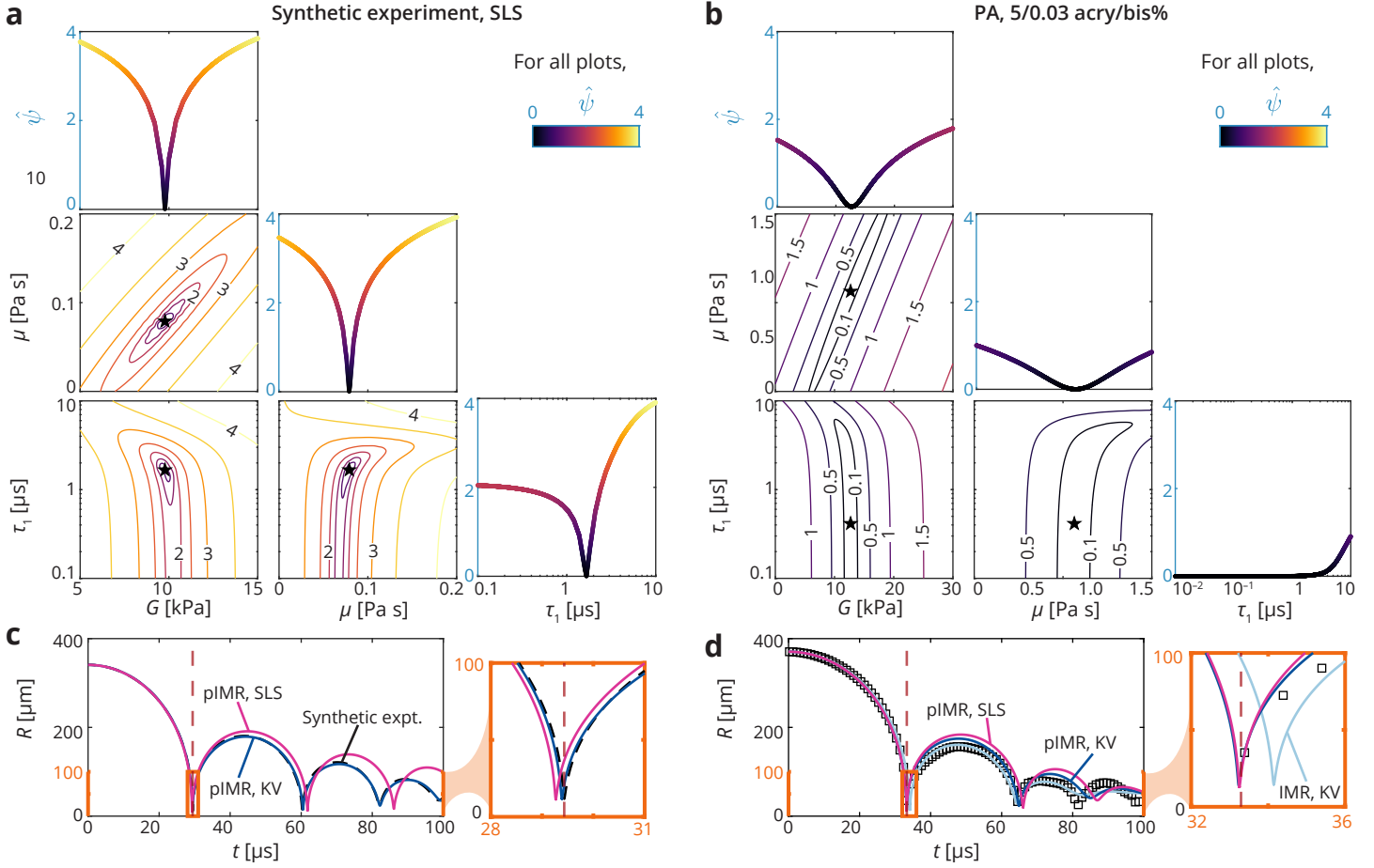
Figure 11: Characterization of SLS model with pIMR. Slices through the 3-parameter normalized cost function $\hat{\psi}$ space for (a) synthetic experiment ($n = 36$) and (b) polyacrylamide gels with 5/0.03% acrylamide/bisacrylamide. The off-diagonal entries show the cost function as a function of two constitutive parameters, with the remaining parameter fixed to the optimized pIMR solution; the diagonal entries show the cost function as a function of a single constitutive parameter. Typical bubble dynamics correspond to the input experiment data and the inverse characterization solutions for (c) synthetic experiment ($n = 36$) and (d) polyacrylamide gels with 5/0.03% acrylamide/bisacrylamide.
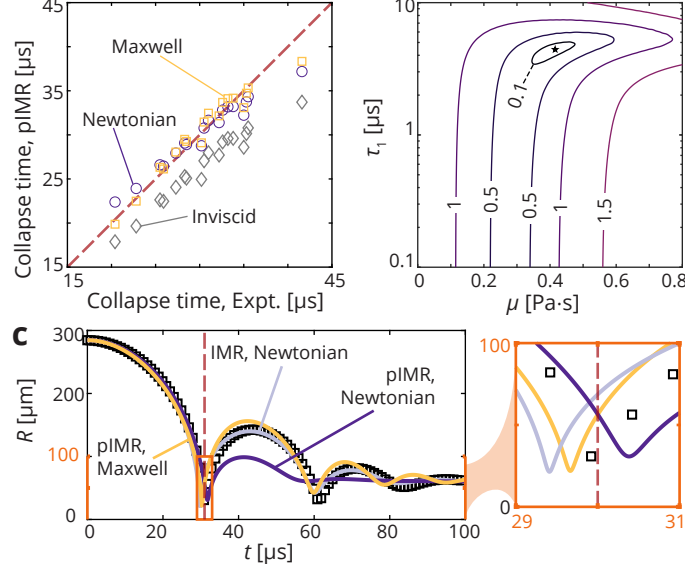
Figure 12: Characterization of 80% (v/v) concentration PEGDA-water mixture. (a) Comparison of measured and predicted collapse time; (b) Normalized cost function $\hat{\psi}$ space for Maxwell model; (c) Typical bubble dynamics corresponding to the input experiment data (hollow squares) and the inverse characterization solutions.

mixture was measured as $(0.122 \pm 0.005)\,\mathrm{Pa \cdot s}$. Using the IMR procedure, a Newtonian model with $\mu = 0.151\,\mathrm{Pa \cdot s}$ was found to minimize the offset between the normalized bubble history $\{t^*, R^*(t^*)\}$ recorded experimentally and simulated by the full-physics model, up to the third oscillation peak. Inverse characterization of the Maxwell model with IMR resulted in a convergence to the Newtonian solution.

In fig. 12 (c), $R(t)$ for a typical experiment is shown with the simulated bubble dynamics using the full-physics model and the optimized constitutive model parameters. Even though the Newtonian viscosity estimated by pIMR results in an error of $\epsilon_\mu = 1.46$ relative to the IMR solution, the pIMR Newtonian solution closely matches the bubble collapse time, with an error of $0.77\,\mathrm{\mu s}$ (relative error: 2.47%). The bubble dynamics of the pIMR Maxwell solution underestimates the collapse time by $0.67\,\mathrm{\mu s}$ (relative error: 2.15%), while the IMR solution resulted in an error of $1.84\,\mathrm{\mu s}$ (relative error: 5.49%).
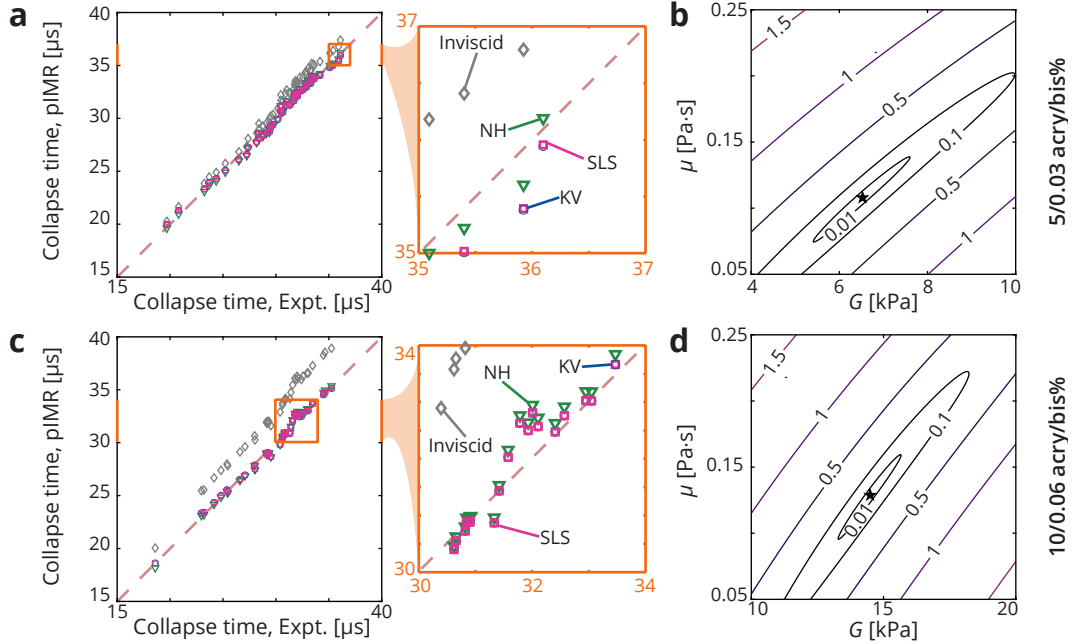
4.3. Characterization of polyacrylamide gels

We characterize polyacrylamide gels with two different concentrations of acrylamide/bisacrylamide. This class of material has been characterized with IMR in past studies [14, 37] and exhibited viscoelastic behaviors that were captured well by the Kelvin–Voigt model.

A total of 52 LIC experiments were performed on specimens with an acrylamide/bisacrylamide concentration of 5/0.03% (v/v), with $R_{\max} = 218.0\text{–}401.3\,\mathrm{\mu m}$ and $\Lambda_{\max} = 6.49\text{–}8.46$. A single-parameter model fit with pIMR resulted in an optimized neo-Hookean solid with $G = 3.11\,\mathrm{kPa}$ and an optimized Newtonian fluid with $\mu \approx 0$, equivalent to an inviscid fluid.

The optimized Kelvin–Voigt parameters were $\{G = 6.52\,\mathrm{kPa}, \mu = 0.109\,\mathrm{Pa \cdot s}\}$ and the optimized SLS parameters were $\{G = 6.36\,\mathrm{kPa}, \mu = 0.113\,\mathrm{Pa \cdot s}, \tau_1 = 0.41\,\mathrm{\mu s}\}$. In fig. 13 (a), the approximated collapse times t_c^{EB} for optimized models are shown vs. the measured collapse time t_c^{Expt} of each experiment. The minimized ψ for the inviscid, neo-Hookean, Kelvin–Voigt, and SLS cases were

Figure 13: Characterization of polyacrylamide gels with pIMR. 5/0.03% (v/v) acrylamide/bisacrylamide: (a) comparison of measured against predicted collapse time and (b) normalized cost function $\hat{\psi}$ space for Kelvin–Voigt model. 10/0.06% (v/v) acrylamide/bisacrylamide: (c) comparison of measured against predicted collapse time and (d) normalized cost function $\hat{\psi}$ space for Kelvin–Voigt model.

calculated to be -2.92, -3.80, -3.88, and -3.88, respectively, and decreasing with the addition of each additional constitutive model parameter, though negligibly with the addition of τ_1. For each LIC experiment, t_c^{Expt} is shorter than what is predicted for an inviscid fluid, again indicating that the ground-state elasticity is more dominant than the material viscosity during the bubble collapse.

Using IMR, optimal Kelvin–Voigt parameters were found to be $\{G = 5.01\,\mathrm{kPa}, \mu = 0.145\,\mathrm{Pa \cdot s}\}$. Inverse characterization of the SLS model with IMR resulted in a convergence to the Kelvin–Voigt solution. With reference to the IMR solution, the errors of the pIMR Kelvin–Voigt results are $\epsilon_G = 0.380$ and $\epsilon_\mu = 0.412$. In fig. 11 (b), with G and μ fixed at the optimized value, $\psi < 0.1$ when $\tau_1 < 1\,\mu\mathrm{s}$, again suggesting that the characterized hydrogel is a Kelvin–Voigt model. The history of $R(t)$ for a typical experiment is shown in fig. 11 (d), along with the simulated bubble dynamics of the optimized models. The bubble dynamics of both the pIMR Kelvin–Voigt and SLS solution matched the collapse time well, with errors of $0.063\,\mu\mathrm{s}$ (relative error: 0.19%) and $0.040\,\mu\mathrm{s}$ (relative error: 0.12%), respectively. The IMR Kelvin–Voigt overestimates the collapse time by $0.84\,\mu\mathrm{s}$ (relative error: 2.5%).

A total of 39 LIC experiments were performed on gels with an acrylamide/bisacrylamide concentration of 10/0.06% (v/v), with $R_{\max} = 215.2$–$416.3\,\mu\mathrm{m}$ and $\Lambda_{\max} = 5.67$–6.76. The optimized model parameters from pIMR are $G = 10.11\,\mathrm{kPa}$ for neo-Hookean, $\mu \approx 0$ again for Newtonian, $\{G = 14.49\,\mathrm{kPa}, \mu = 0.130\,\mathrm{Pa \cdot s}\}$ for Kelvin–Voigt, and $\{G = 14.50\,\mathrm{kPa}, \mu = 0.152\,\mathrm{Pa \cdot s}, \tau_1 = 0.80\,\mu\mathrm{s}\}$ for SLS. The minimized ψ for the inviscid, neo-Hookean, Kelvin–Voigt and SLS cases were -2.06, -3.78, -3.89, and -3.89. The contribution of material viscoelasticity to the bubble collapse time is stronger than what was observed in the 5/0.03% (v/v) acrylamide/bisacrylamide samples analyzed above, as shown by the greater decrease of ψ between the inviscid and optimized neo-Hookean

models. By comparing fig. 13 (b) against fig. 13 (a), we also observe a larger deviation of the inviscid model collapse time (gray diamond) from the red dashed line corresponding to a perfect fit of the experimental collapse time. With IMR, the optimal set of Kelvin–Voigt parameters was found to be $\{G = 12.02\,\text{kPa}, \mu = 0.115\,\text{Pa} \cdot \text{s}\}$. With reference to the IMR solution, the errors of the pIMR Kelvin–Voigt results are $\epsilon_G = 0.270$ and $\epsilon_\mu = 0.177$.

5. Discussion

The inverse characterization examples presented in Section 4 have confirmed the effectiveness of pIMR at rapidly estimating Kelvin–Voigt model parameters from the scaling of the bubble collapse time t_c across a batch of experiments with differing bubble sizes $R_{\max}$ and amplification factors $\Lambda_{\max}$. For the 52-sample batch of polyacrylamide gel (5/0.03% (v/v) acryl/bis) experiments, the optimal Kelvin–Voigt parameters for all samples were determined within 1 second of computation on a workstation (Intel Core i7 14700K). Using the full-physics model, approximately 10 seconds of computational time are required to simulate the bubble dynamics up to the fourth peak of oscillation for each set of input parameters describing the material viscoelasticity and the bubble's initial and equilibrium conditions in each experiment. The computational cost is amplified as the simulation is repeated for combinations of input parameters.

The estimation of viscoelastic properties from collapse time also relaxes the strict requirements that IMR previously placed on the optical turbidity of the characterized material. With a decreased frame rate and an increased exposure time per frame, bright-field videography can still be used to measure the maximum and equilibrium radii of the bubble in an optically turbid material. Since the bubble collapse coincides with the emission of shockwave, its occurrence can be captured with methods other than the optical strategy introduced in Section 2.4. For example, integrated circuit piezoelectric transducers, commonly used in shock tube [38–40] and Kolsky bar [7, 41] experiments, can be integrated in the LIC experiment setup to detect pressure spikes due to the bubble collapse. Past studies of laser- and ultrasound-induced cavitation [19, 42, 43] have also used hydrophones to acquire acoustic signals and identify the occurrences of shockwave-emitting collapse events.

Comparisons of the experimentally measured collapse time and the predicted collapse time of the optimized constitutive models in the polyacrylamide gel experiments suggest that the material viscosity contributes a comparatively smaller amount than the elasticity to the bubble collapse time in this class of materials. The minimized cost function ψ for the neo-Hookean model is only slightly higher than those of the Kelvin–Voigt and SLS models. However, a close inspection of fig. 13 (a) and (c) also reveals that the optimized neo-Hookean model underestimated the collapse time in experiments with small $R_{\max}$ and overestimated the collapse time in experiments with large $R_{\max}$. The addition of material viscosity improved the agreement between the measured and predicted collapse time values since $\overline{f}_v^*$ increases in magnitude with smaller Re; smaller $R_{\max}$ for a fixed μ. To more clearly distinguish the contribution of viscosity on the collapse time and fully use the pIMR procedure proposed, a broader range of $R_{\max}$ should be surveyed. However, the maximum bubble radius $R_{\max}$ currently achievable in our experiments is bounded by the current geometric limitations of our setup. The range could indeed be broadened with longer-focal-length objectives permitting larger samples and maximum bubble sizes or sub-nanosecond laser pulses to produce more reliable small bubble events.

The cuvette size limits the upper bound of bubble size to maintain spherical bubbles consistent with the theoretical bubble dynamics model adopted. The minimum size of the $R_{\max}$ is practically limited by a combination of the numerical aperture of the converging optical objective, laser profile,

and requirement to see the emitted shockwave on collapse for time assessment. As a result, the hydrogel experiments presented above spanned a range of R_{max} with an upper-to-lower-bound ratio of approximately 2.

The computational cost of pIMR for the SLS model is presently closer to that of IMR, on the order of hours for the 52-sample polyacrylamide gel (5/0.03% (v/v) acryl/bis) experiments presented in Section 4. The evaluation of $f_{\mathrm{m,o}}^{*}$ in (28) currently relies on an iterative procedure, with each iteration requiring a numerical simulations of the bubble growth process. To achieve a rapid inverse characterization, improvements are needed for the parsimonious quantification of the SLS model parameters. Additional measurable parameters may be harnessed in addition to the initial collapse time considered in the present work for a more effective parsimonious characterization of the SLS models. For example, the optimized Kelvin–Voigt and SLS solutions shown in fig. 11 (c) result in bubble dynamics that diverge more discernibly from each other after the initial collapse. Parameters such as the maximum radius at the second peak and the time of the second collapse may be valuable for the inverse characterization of SLS materials.

6. Conclusion

We present the pIMR, a parsimonious enhancement of the IMR that rapidly characterizes the local viscoelastic properties of soft materials from laser-induced cavitation experiments. This new procedure is possible due to experimental advancements in estimating the collapse time of a laser-induced cavity, coupled with a theoretical energy balance analysis. We make an ansatz to a modified potential energy through linearizing effects within the Keller–Miksis equation. This ansatz allows the collapse time approximation to include viscoelastic parameters, surface tension, bubble pressure, and finite wave speed. In our approach, we do not introduce empirical fitting parameters in the energy balance analysis to improve its agreement with the full-physics bubble dynamics model. These approximate models for the collapse time were shown to perform well in predicting the collapse time from simulations of the Keller–Miksis equation over a parameter space that is experimentally relevant to inertial microcavitation within soft materials.

The proposed procedure pares down the space upon which we seek the global optima of viscoelastic model parameters. As an example, a Kelvin–Voigt model with elastic and viscous moduli of the orders of $10\,\mathrm{kPa}$ and $0.1\,\mathrm{Pa\cdot s}$, respectively, are reproduced through tens of synthetic LIC experiments, with multiplicative error factors below 1.1 for both parameters. Experimental characterization of viscous fluid and hydrogel specimens resulted in optimized Kelvin–Voigt parameters that closely matched the results of the IMR procedure while reducing the computational cost of post-processing to a few seconds. With reduced reliance on measurements of the full bubble dynamics, pIMR also potentially enables the characterization of optically turbid materials with LIC experiments aided by the acoustic detection of shock waves.

We note the limitations of the proposed procedure. Although our energy balance analysis can approximate the bubble collapse time in viscoelastic models with Maxwell-type relaxation, the dependence of the bubble dynamics on the initial bubble growth results in an inverse characterization procedure that still relies on numerical simulations. We envision that an inverse characterization procedure considering measurable parameters in the post-collapse bubble dynamics can address this issue. Moreover, experimental adjustments (e.g., larger sample sizes and objectives with longer focal lengths) would be needed to increase the range of maximum bubble size achievable in the LIC experiments, which in turn would broaden the range of material viscosity values identifiable via pIMR.

Conflict of Interest

The authors have no known conflicts of interest associated with this publication, and there has been no significant financial support for this work that could have influenced its outcome.

Data availability

The code for pIMR is available at: https://github.com/InertialMicrocavitationRheometry/parsimonious_IMR.

References

[1] B. A. Abeid, M. L. Fabiilli, M. Aliabouzar, J. B. Estrada, Experimental & numerical investigations of ultra-high-speed dynamics of optically induced droplet cavitation in soft materials, Journal of the Mechanical Behavior of Biomedical Materials **160** (2024) 106776.

[2] J. B. Estrada, H. C. Cramer III, M. T. Scimone, S. Buyukozturk, C. Franck, Neural cell injury pathology due to high-rate mechanical loading, Brain Multiphysics **2** (2021) 100034.

[3] M. R. Bailey, R. O. Cleveland, T. Colonius, L. A. Crum, A. P. Evan, J. E. Lingeman, J. A. McAteer, O. A. Sapozhnikov, J. Williams, Cavitation in shock wave lithotripsy: the critical role of bubble activity in stone breakage and kidney trauma, in: IEEE Symposium on Ultrasonics, 2003, volume 1, IEEE, 2003, pp. 724–727.

[4] Z. Xu, J. B. Fowlkes, E. D. Rothman, A. M. Levin, C. A. Cain, Controlled ultrasound tissue erosion: The role of dynamic interaction between insonation and microbubble activity, The Journal of the Acoustical Society of America **117** (2005) 424–435.

[5] J. E. Parsons, C. A. Cain, G. D. Abrams, J. B. Fowlkes, Pulsed cavitational ultrasound therapy for controlled tissue homogenization, Ultrasound in medicine & biology **32** (2006) 115–129.

[6] A. Vogel, S. Busch, U. Parlitz, Shock wave emission and cavitation bubble generation by picosecond and nanosecond optical breakdown in water, The Journal of the Acoustical Society of America **100** (1996) 148–165.

[7] W. W. Chen, Experimental methods for characterizing dynamic response of soft materials, Journal of Dynamic Behavior of Materials **2** (2016) 2–14.

[8] J. A. Zimberlin, N. Sanabria-DeLong, G. N. Tew, A. J. Crosby, Cavitation rheology for soft materials, Soft Matter **3** (2007) 763–767.

[9] S. Kundu, A. J. Crosby, Cavitation and fracture behavior of polyacrylamide hydrogels, Soft Matter **5** (2009) 3963–3968.

[10] M. P. Milner, S. B. Hutchens, A device to fracture soft solids at high speeds, Extreme Mechanics Letters **28** (2019) 69–75.

[11] M. P. Milner, S. B. Hutchens, Multi-crack formation in soft solids during high rate cavity expansion, Mechanics of Materials **154** (2021) 103741.

[12] S. Raayai-Ardakani, T. Cohen, Capturing strain stiffening using volume controlled cavity expansion, Extreme Mechanics Letters **31** (2019) 100536.

[13] S. Chockalingam, C. Roth, T. Henzel, T. Cohen, Probing local nonlinear viscoelastic properties in soft materials, Journal of the Mechanics and Physics of Solids (2020) 104172.

[14] J. B. Estrada, C. Barajas, D. L. Henann, E. Johnsen, C. Franck, High strain-rate soft material characterization via inertial cavitation, Journal of the Mechanics and Physics of Solids **112** (2018) 291–317.

[15] J. Yang, H. C. Cramer III, C. Franck, Extracting non-linear viscoelastic material properties from violently-collapsing cavitation bubbles, Extreme Mechanics Letters **39** (2020) 100839.

[16] J.-S. Spratt, M. Rodriguez, K. Schmidmayer, S. H. Bryngelson, J. Yang, C. Franck, T. Colonius, Characterizing viscoelastic materials via ensemble-based data assimilation of bubble collapse observations, Journal of the Mechanics and Physics of Solids **152** (2021) 104455.

[17] A. McGhee, J. Yang, E. Bremer, Z. Xu, H. Cramer III, J. Estrada, D. Henann, C. Franck, High-speed, full-field deformation measurements near inertial microcavitation bubbles inside viscoelastic hydrogels, Experimental Mechanics **63** (2023) 63–78.

[18] J. B. Keller, M. Miksis, Bubble oscillations of large amplitude, The Journal of the Acoustical Society of America **68** (1980) 628–633.

[19] I. Akhatov, O. Lindau, A. Topolnikov, R. Mettin, N. Vakhitova, W. Lauterborn, Collapse and rebound of a laser-induced cavitation bubble, Physics of Fluids **13** (2001) 2805–2819.

[20] R. Nigmatulin, N. Khabeev, F. Nagiev, Dynamics, heat and mass transfer of vapour-gas bubbles in a liquid, International Journal of Heat and Mass Transfer **24** (1981) 1033–1044.

[21] A. Prosperetti, L. A. Crum, K. W. Commander, Nonlinear bubble dynamics, The Journal of the Acoustical Society of America **83** (1988) 502–514.

[22] C. Barajas, E. Johnsen, The effects of heat and mass diffusion on freely oscillating bubbles in a viscoelastic, tissue-like medium, The Journal of the Acoustical Society of America **141** (2017) 908–918.

[23] X. Yang, C. C. Church, A model for the dynamics of gas bubbles in soft tissue, The Journal of the Acoustical Society of America **118** (2005) 3595–3606.

[24] C. Hua, E. Johnsen, Nonlinear oscillations following the rayleigh collapse of a gas bubble in a linear viscoelastic (tissue-like) medium, Physics of Fluids **25** (2013) 083101.

[25] M. Warnez, E. Johnsen, Numerical modeling of bubble dynamics in viscoelastic media with relaxation, Physics of Fluids **27** (2015) 063103.

[26] R. Gaudron, M. Warnez, E. Johnsen, Bubble dynamics in a viscoelastic medium with nonlinear elasticity, Journal of Fluid Mechanics **766** (2015).

[27] E. Bremer-Sai, J. Yang, A. McGhee, C. Franck, Ballistic and blast-relevant, high-rate material properties of physically and chemically crosslinked hydrogels, Experimental Mechanics **64** (2024) 587–592.

[28] J. W. Strutt, Viii. on the pressure developed in a liquid during the collapse of a spherical cavity, The London, Edinburgh, and Dublin Philosophical Magazine and Journal of Science **34** (1917) 94–98.

[29] C. E. Brennen, Cavitation and bubble dynamics, Cambridge University Press, 2014.

[30] A. T. Preston, Modeling heat and mass transfer in bubbly cavitating flows and shock waves in cavitating nozzles, California Institute of Technology, 2004.

[31] J. Yang, A. McGhee, G. Radtke, M. Rodriguez, C. Franck, Estimating viscoelastic, soft material properties using a modified rayleigh cavitation bubble collapse time, Physics of Fluids **36** (2024).

[32] J. R. Sukovich, S. C. Haskell, Z. Xu, T. L. Hall, A cost-effective, multi-flash,"ghost" imaging technique for high temporal and spatial resolution imaging of cavitation using "still-frame" cameras, The Journal of the Acoustical Society of America **147** (2020) 1339–1343.

[33] J. R. Tse, A. J. Engler, Preparation of hydrogel substrates with tunable mechanical properties, Current protocols in cell biology **47** (2010) 10–16.

[34] S. Buyukozturk, J.-S. Spratt, D. Henann, T. Colonius, C. Franck, Particle-assisted laser-induced inertial cavitation for high strain-rate soft material characterization, Experimental Mechanics **62** (2022) 1037–1050.

[35] J. C. Lagarias, J. A. Reeds, M. H. Wright, P. E. Wright, Convergence properties of the nelder–mead simplex method in low dimensions, SIAM Journal on optimization **9** (1998) 112–147.

[36] M. D. McKay, R. J. Beckman, W. J. Conover, A comparison of three methods for selecting values of input variables in the analysis of output from a computer code, Technometrics **42** (2000) 55–61.

[37] A. Tzoumaka, J. Yang, S. Buyukozturk, C. Franck, D. L. Henann, Modeling high strain-rate microcavitation in soft materials: the role of material behavior in bubble dynamics, Soft Matter **19** (2023) 3895–3909.

[38] S. Bentil, K. Ramesh, T. Nguyen, A dynamic inflation test for soft materials, Experimental Mechanics **56** (2016) 759–769.

[39] R. S. Salzar, D. Treichler, A. Wardlaw, G. Weiss, J. Goeller, Experimental investigation of cavitation as a possible damage mechanism in blast-induced traumatic brain injury in post-mortem human subject heads, Journal of neurotrauma **34** (2017) 1589–1602.

[40] J. L. Marsh, L. Zinnel, S. A. Bentil, Cavitation bubble dynamics using a shock tube model for blast injury research, Journal of Dynamic Behavior of Materials (2024) 1–17.

[41] H. Saraf, K. Ramesh, A. Lennon, A. Merkle, J. Roberts, Measurement of the dynamic bulk and shear response of soft human tissues, Experimental mechanics **47** (2007) 439–449.

[42] J. R. Sukovich, Z. Xu, Y. Kim, H. Cao, T.-S. Nguyen, A. S. Pandey, T. L. Hall, C. A. Cain, Targeted lesion generation through the skull without aberration correction using histotripsy, IEEE transactions on ultrasonics, ferroelectrics, and frequency control **63** (2016) 671–682.

[43] J. R. Sukovich, J. J. Macoskey, J. E. Lundt, T. I. Gerhardson, T. L. Hall, Z. Xu, Real-time transcranial histotripsy treatment localization and mapping using acoustic cavitation emission feedback, IEEE transactions on ultrasonics, ferroelectrics, and frequency control **67** (2020) 1178–1191.

[44] E. Traldi, M. Boselli, E. Simoncelli, A. Stancampiano, M. Gherardi, V. Colombo, G. S. Settles, Schlieren imaging: a powerful tool for atmospheric plasma diagnostic, EPJ Techniques and Instrumentation **5** (2018) 1–23.

[45] V. Agrež, T. Požar, R. Petkovšek, High-speed photography of shock waves with an adaptive illumination, Optics letters **45** (2020) 1547–1550.

Appendix A. Viscoelastic stress field and stress integral in a Maxwell material

To clarify the underlying physics, dimensional parameters will be used below. We denote the equilibrium radius of the spherical bubble as R_0 and the referential radial coordinate for a material point in the surrounding viscoelastic medium to be $r_0 \in [R_0, \infty)$, measured from the center of the bubble. The deformed coordinate of a material point r_0 at time t is $r = (r_0^3 + R(t)^3 - R_0^3)^{1/3}$. We define the hoop stretch, $\lambda(r_0, t) = r(r_0, t)/r_0$, which is equal to $\Lambda(t) = R(t)/R_0$ at the bubble wall. This results in the deformation gradient with the following components in the spherical coordinate system:

$$[\mathbf{F}] = \begin{bmatrix} \lambda^{-2} & 0 & 0 \\ 0 & \lambda & 0 \\ 0 & 0 & \lambda \end{bmatrix}. \tag{A.1}$$

In terms of rheological schematics, a Maxwell element consists of an elastic "spring" response in series with a viscous "dashpot" response. Under finite deformation, we multiplicatively decompose the deformation gradient into elastic and viscous distortions, $\mathbf{F} = \mathbf{F}^{\mathrm{e}}\mathbf{F}^{\mathrm{v}}$, which corresponds to a decomposition of hoop stretch $\lambda = \lambda^{\mathrm{e}}\lambda^{\mathrm{v}}$ for the cavitation problem considered in the present study.

For ease of mathematical manipulation, we employ the logarithmic strain,

$$\mathbf{E}^{\mathrm{e}} = \frac{1}{2}\ln\left(\mathbf{F}^{\mathrm{e}\top}\mathbf{F}^{\mathrm{e}}\right), \tag{A.2}$$

and express the free energy density of the elastic response as $\psi(\mathbf{E}^{\mathrm{e}}) = G_1|\mathrm{dev}(\mathbf{E}^{\mathrm{e}})|^2$, where G_1 is the associated elastic shear modulus.

The non-zero components of the deviatoric Cauchy stress in the Maxwell element are, $s_{rr} = -2s_{\theta\theta} = -4G_1 \ln \lambda^{\mathrm{e}}$. For the viscous part of the Maxwell element, we adopt the Newtonian fluid formulation with $\mathbf{s}^{\mathrm{v}} = \mu \, \mathrm{dev}(\dot{\mathbf{F}}^{\mathrm{v}}\mathbf{F}^{\mathrm{v},-1} + \mathbf{F}^{\mathrm{v},-\top}\dot{\mathbf{F}}^{\mathrm{v},\top})$, where μ is the viscous shear modulus. Given stress equivalence in the elastic and viscous parts of the Maxwell element, we have the governing

equation,

$$\frac{\dot{\lambda}}{\lambda} - \frac{\dot{\lambda}^{\mathrm{e}}}{\lambda^{\mathrm{e}}} = \frac{1}{\tau_1} \ln \lambda^{\mathrm{e}} \tag{A.3}$$

where $\tau_1 = \mu/G_1$ is an inherent time scale describing stress relaxation. The stress at a material point is, then,

$$s_{rr}(r_0, t) = -4G_1 \int_{-\infty}^{t} e^{(\xi-t)/\tau_1} \frac{\dot{\lambda}(r_0, \xi)}{\lambda(r_0, \xi)} \mathrm{d}\xi = -4G_1 \int_{-\infty}^{t} e^{(\xi-t)/\tau_1} \frac{\dot{r}(r_0, \xi)}{r(r_0, \xi)} \mathrm{d}\xi. \tag{A.4}$$

Accordingly, the stress integral in the Keller–Miksis equation can be evaluated for the Maxwell element:

$$S = \int_{R}^{\infty} \frac{3}{r} s_{rr}(r_0(r, t), t) \mathrm{d}r = -12G_1 \int_{-\infty}^{t} e^{(\xi-t)/\tau_1} \frac{R^2(\xi) \dot{R}(\xi) \ln\left(R(\xi)/R(t)\right)}{R^3(\xi) - R^3(t)} \mathrm{d}\xi. \tag{A.5}$$

When the characteristic time scale of the bubble oscillation is longer than the time scale of the exponential relaxation of the Maxwell material, τ_1, we approximate $R(y) \approx R(\xi)$ in (A.5). This approximation leads to the stress integral expression for the linear Maxwell model,

$$S = -4G_1 \int_{-\infty}^{t} e^{(\xi-t)/\tau_1} \frac{\dot{R}(\xi)}{R(\xi)} \mathrm{d}\xi, \tag{A.6}$$

which conveniently satisfies the ODE,

$$S + \tau_1 \dot{S} = -4\mu \dot{R}/R. \tag{A.7}$$

For the energy balance analysis presented in Section 2.2, this expression is easier to manipulate than (A.5). For the typical range of μ and τ_1 considered in the present study, we have found that the bubble dynamics resulting from the linear Maxwell and the finite deformation Maxwell models agree well during the initial collapse.

Due to the fading memory of the Maxwell material, a non-zero stress integral remains at the end of the bubble growth phase, contributing to the ensuing bubble collapse. We presently do not have an analytical model to quantify this initial value of the stress integral. Instead, we advance the ODE (A.7) from the beginning of the growth phase, with initial conditions R_0 and $\dot{R} = V_0 > 0$, and evaluate S when $\dot{R}$ decreases to 0 at the end of the growth phase. A Nelder–Mead direct search process [35] is used to iteratively solve for V_0 to minimize $|R - R_{\mathrm{max}}|$ at the end of the growth phase. Heat and mass transfer in the bubble content and surface tension of the bubble wall are neglected in these simulations of the bubble growth phase.

Appendix B. Experimental methods

Our setup generates, records, and profiles pulses of single LIC bubble events in soft materials using a combination of a pulsed, Q-switched, user-adjustable 1–25 mJ, frequency-doubled 532 nm Nd:YAG laser (Continuum Minilite II, San Jose, CA) and a high-speed imaging camera (HPV-X2; Shimadzu, Kyoto, Japan). The setup is triggered using an 8-channel pulse/delay generator (Model 577; Berkeley Nucleonics, San Rafael, CA) according to a customized pre-programmed pulse sequence. The pulse sequence was validated using an oscilloscope (P2025; Berkely Nucleonics). Sequential triggering

signals fire two single pulses: the first triggers the laser's flash lamp, and the second fires the Q-switch. The last two triggering signals are sent to a beam profiler (BC106N-VIS; Thorlabs) and the high-speed camera. The backside of the sample is illuminated with the aid of a 640 nm monochromatic ultra-high-speed strobed diode laser (Cavilux Smart UHS; Cavitar, Tampere, Finland). The high-speed camera sync-out signal triggers the illumination laser. The laser beam/pulse was aligned to the back apparatus of a 10X/0.25 High-Power MicroSpot Focusing Objective (LMH-10X-532; Thorlabs, Newton, NJ) using three reflective broadband dielectric mirrors (BB1-E02; Thorlabs, Newton, NJ), three short-pass dichroic mirrors, a beam-sampler, and a spatial light modulator (SLM) (Holoeye, Berlin, Germany). The first dichroic mirror (DMSP605; Thorlabs, Newton, NJ) is used for the beam alignment in conjunction with a continuous exposure Collimated Laser Diode Module (CPS635R; Thorlabs, Newton, NJ). A 2X fixed magnification beam-expander (GBE02-A; Thorlabs, Newton, NJ) helps distribute the collimated beam on a larger area and minimizes any potential damage to the SLM and focusing objective lens at the back aperture. The second high-pass dichroic mirror (DMSP550; Thorlabs, Newton, NJ), which has a cutoff wavelength of 550 nm, was used to filter infrared wavelengths and discard them into a beam-block (LB2; Thorlabs, Newton, NJ). The visible beam is then reflected onto a spatial light modulator, allowing for higher control over the last pulse shape and energy. Last, the beam is split before it reaches the focusing objective using a beam sampler lens (BSF10-A; Thorlabs, Newton, NJ). Approximately 0.5% of the split beam is reflected towards a beam profiler (BC106N-VIS; Thorlabs, Newton, NJ) to assess the pulse quality and measure its energy. The remaining 99.5% of the beam continues to the focusing objective through the third dichroic mirror (DMSP550; Thorlabs, Newton, NJ), which also has a cutoff wavelength of 550 nm, allowing the cavitation laser (532 nm) to pass while reflecting the illumination laser light (640 nm). The focusing objective focuses the beam at the microcavitation imaging plane.

The microcavitation event is performed at 1 million frames per second (Mfps) using a Shimadzu HPV-X2 (Tokyo, Japan) high-speed imaging camera, illuminated by CAVILUX Smart UHS (Tampere, Finland) laser, and through both, the cavitation objective and an Olympus Plan 10X-0.25 Achromat imaging objective (RMS10X; Thorlabs, Newton, NJ). The data is analyzed using our in-house Matlab image processing code. To measure the wave speed in the medium, we deployed two imaging techniques simultaneously: laser shadowgraph [44] and ghost imaging [45]. Shadowgraph imaging is performed by manipulating the backlighting path to capture density variation due to the compressive shockwave. The physical location of the pressure wave is then estimated during the bubble's cavitation and collapse. Ghost imaging is achieved by triggering the strobed backlight a user-defined number of times per camera exposure, usually 2 or 3 per frame.